UNLV Theses, Dissertations, Professional Papers, and Capstones

May 2018

Petrology and Geochemistry of the Enriched Poikilitic Shergottite Northwest Africa 10169: Insight into the Martian Interior

Logan Matthew Combs
lcombs1105@gmail.com

PETROLOGY AND GEOCHEMISTRY OF THE ENRICHED POIKILITIC SHERGOTTITE

NORTHWEST AFRICA 10169: INSIGHT INTO THE MARTIAN INTERIOR

By

Logan M. Combs

Bachelor of Science – Geology
University of Tennessee Knoxville
2014

A thesis submitted in partial fulfillment
of the requirements for the

Master of Science – Geoscience

Department of Geoscience
College of Science
The Graduate College

University of Nevada, Las Vegas
May 2018

Thesis Approval

The Graduate College
The University of Nevada, Las Vegas

April 10, 2018

This thesis prepared by

Logan M. Combs

entitled

Petrology and Geochemistry Of The Enriched Poikilitic Shergottite
Northwest Africa 10169: Insight Into The Martian Interior

is approved in partial fulfillment of the requirements for the degree of

Master of Science – Geoscience
Department of Geoscience

Arya Udry, Ph.D.   Kathryn Hausbeck Korgan, Ph.D.
Examination Committee Chair   *Graduate College Interim Dean*

Shichun Huang, Ph.D.
Examination Committee Member

Elisabeth Hausrath, Ph.D.
Examination Committee Member

Jason Steffen, Ph.D.
Graduate College Faculty Representative

ABSTRACT

The martian meteorite Northwest Africa (NWA) 10169 is classified as a new member of the geochemically enriched poikilitic shergottites, based on mineral composition, Lu-Hf isotope systematics, and rare earth element (REE) composition. Akin to other poikilitic shergottites, it shows a similar bimodal texture to other enriched and intermediate poikilitic shergottites. In addition, olivine and pyroxene in the poikilitic zone have higher Mg#'s (Mg/Mg+Fe) than those in the interstitial areas, suggesting that the poikilitic texture represents early-stage crystallization, opposed to late-stage non-poikilitic crystallization. Calculated fO_2 values are reduced (FMQ -2.3 $\pm$ 0.23) within the poikilitic texture, and more oxidized (FMQ -1.07 $\pm$ 0.14) within the interstitial areas likely representing auto-oxidation and degassing during magma crystallization. Melt inclusions within olivine crystals provide snapshots of magma composition throughout parent melt evolution. The calculated parental melt compositions share evolution trends with the enriched olivine-phyric shergottite Larkman Nunatuk (LAR) 06319, and suggest that two melts (K-poor and K-rich) were involved in the formation of NWA 10169, likely representing interaction with a metasomatized melt during the entrapment of the K-rich melt inclusions. The Lu-Hf crystallization age for NWA 10169 is 167 $\pm$ 31 Ma, consistent with the other enriched shergottites. Based on the isochron initial $^{176}Hf/^{177}Hf$ value, the modeled the source $^{176}Lu/^{177}Hf$ composition for NWA 10169 is 0.02748 $\pm$ 0.00037, identical within error to the source compositions of the enriched shergottites Shergotty, Zagami, LAR 06319, NWA 4468, and Roberts Massif (RBT) 04262, suggesting a shared, long-lived geochemical source, distinct from the source tapped by Los Angeles, NWA 856, and NWA 7320. This study reveals that at least two sources are responsible for the enriched shergottites, and a more heterogeneous martian mantle than previously thought. Additionally, the shared source with NWA 10169, coupled with consistent crystallization ages and magmatic

histories indicates that a common magmatic system on Mars is likely responsible for the formation of this group of shergottites.

ACKNOWLEDGEMENTS

TABLE OF CONTENTS

LIST OF TABLES

LIST OF FIGURES

1. INTRODUCTION

Shergottites are the most abundant of the three main groups of martian meteorites (shergottites, nakhlites, and chassignites), accounting for ~ 90% of the known samples. At this moment, martian meteorites represent the only physical samples of Mars on Earth, and as such, their study is crucial to further our understanding of the geology and magmatic processes of Mars. Shergottites, on the basis of their textural and mineralogical characteristics are divided into four groups: The basaltic, olivine-phyric, poikilitic, and gabbroic shergottites (e.g., McSween and Treiman, 1998; Goodrich, 2002; Bridges and Warren, 2006; Udry et al., 2017). The basaltic and olivine-phyric shergottites are thought to represent hypabyssal to surficial extrusive rocks, while the poikilitic and gabbroic shergottites are thought to represent intrusive rocks emplaced at depth in the martian crust (e.g., Goodrich, 2002; Filiberto et al., 2014; Udry et al., 2017). Poikilitic shergottites, formerly known as "lherzolitic" shergottites, consist of >20% of the martian meteorite collection; to date, 26 have been recovered. They are characterized by their bimodal texture (Fig. 1), comprised of a poikilitic texture and an interstitial non-poikilitic texture. The poikilitic texture is defined by large, anhedral, zoned (low-Ca cores to high-Ca rims) pyroxene oikocrysts, which enclose rounded olivine chadacrysts (Figs. 1 and 2). The non-poikilitic texture is characterized by an assemblage of subequigranular maskelynite, pyroxene, and olivine. This zone likely formed at the late-stage of bulk rock crystallization, and is interpreted to represent the composition of the residual magma (Howarth et al., 2014). A polybaric formation model has been proposed for the formation of the poikilitic shergottites, involving the formation and accumulation of pyroxene oikocrysts within a magma staging chamber, and the subsequent formation of the interstitial non-poikilitic texture following the rise of the magma towards the surface (Howarth et al., 2014). This

1

unique texture and crystallization process amongst shergottites allow us to investigate the evolution of the parental magma from early to late-stage crystallization.

Shergottites are also divided into three geochemical groups (enriched, intermediate, and depleted) on the basis of their relative light rare earth element (LREE) enrichment; initial ε^{143}Nd and ε^{176}Hf compositions; and δ^{18}O values (e.g., Bridges and Warren, 2006; DeBaille et al., 2008; McSween, 2015). These observed geochemical variations within the shergottite suite have been interpreted to have arisen through sampling of two distinct geochemical reservoirs on Mars. The first reservoir is depleted in LREE (low La/Yb); relatively reduced; has more radiogenic compositions (high ε^{143}Nd and ε^{176}Hf values); and low δ^{18}O values, consistent with a depleted mantle source reservoir. The second reservoir is enriched in LREE (high La/Yb); relatively oxidized; has less radiogenic compositions (low ε^{143}Nd and ε^{176}Hf values); and high δ^{18}O values. The identity of this reservoir, and its location within the martian interior, be it an enriched mantle reservoir, assimilated crust, or both, remains enigmatic (e.g., Herd et al., 2002; Symes et al., 2008; Basu Sarbadhikari et al., 2011; Peters et al., 2015). As of yet, the poikolitic shergottites are represented by two of the three geochemical groups, the intermediate and the enriched. Before 2010, the only poikilitic shergottites recovered had been classified as geochemically intermediate (McSween et al., 1979; Harvey et al., 1993; Mikouchi and Miyamoto, 1996; Gleason et al., 1997; Ikeda, 1997; Goodrich 2003; Hsu et al., 2004; Gillet et al., 2005; Lin et al., 2005; Walton et al., 2012). Recently however, the enriched poikilitic shergottites, which show similar petrologic characteristics to the intermediate poikilitic shergottites, yet distinct geochemical source characteristics have been studied (Usui et al., 2010; Jiang and Hsu, 2012; Lin et al., 2013; Howarth et al., 2014, 2015).

Crystallization and cosmic ray exposure (CRE) ages suggest that there are two groups within the enriched poikilitic shergottites, one related to the enriched olivine-phyric and basaltic shergottites, and the other related to the intermediate poikilitic shergottites. Robert Massif (RBT) 04261/2 and Northwest Africa (NWA) 4468, the only enriched poikilitic shergottites to have both their CRE and crystallization ages determined, yielded crystallization ages of 225 ± 21 Ma and 150 ± 29 Ma, respectively, and ejection ages of ~ 3 Ma (Borg et al., 2008; Lapen et al., 2008; Nishiizumi and Caffee, 2010; Niihara, 2011; Wieler et al., 2016). These ejection and crystallization ages, along with the crystallization ages of the intermediate poikilitic shergottites (~ 180 Ma), overlap with the ejection and crystallization ages of the enriched basaltic shergottites, of ~ 3 Ma and ~ 165 to 177 Ma, respectively (Nyquist et al., 2001; Christen et al., 2005; Usui et al., 2010). Two other enriched poikilitic shergottites, NWA 6342 and NWA 7397, have had their CRE ages determined and yielded ages of ~ 4.5 Ma, coinciding with the ejection ages of the intermediate poikilitic shergottite suite (~ 4 to 5 Ma) (Nyquist et al., 2001; Christen et al., 2005; Wieler et al., 2016). Thus, although intermediate and enriched poikilitic shergottites have similar textures, some enriched poikilitic shergottites may be spatially related to basaltic shergottites.

Here I present bulk and mineral major and trace element compositions; estimated conditions of formation; parent melt composition from melt inclusions; and Lu-Hf ages and Sm-Nd isotopic compositions for the poikilitic shergottite NWA 10169. Northwest Africa 10169 is a 22 g meteorite that was found in the Laayoune region of Western Sahara in January, 2015 and identified as a poikilitic shergottite in July, 2015 (Hewins and Zanda, 2015). The geochemistry, mineralogy, and texture of this meteorite indicate that NWA 10169 is a new member of the geochemically enriched poikilitic shergottites. By conducting a comprehensive petrologic study

of a member of this rare group, I aim to gain a deeper understanding of the source of the enriched

shergottites and the formation of this group of meteorites.

2. ANALYTICAL METHODS

2.1 Electron microprobe analyses

2.1.1 In situ major and minor element analyses

In situ and textural analyses in this study were performed on two thin sections (S1 and S2), cut from a chip of NWA 10169 (Fig. 1). Major and minor element compositions of the minerals of NWA 10169 were measured through electron microprobe (EMP) analysis using the *JEOL JXA-8900* Superprobe at the University of Nevada Las Vegas (UNLV). Analyses were performed with an accelerating voltage of 15 kV, a beam current of 20 nA, a beam diameter of 5 µm, and standard PAP corrections for all phases but maskelynite and glass. The beam current was decreased to 10 nA for maskelynite and glass analyses to prevent volatilization. Peak count times were 10 s for Na and F; and 30 s for Ca, Mg, Al, Fe, Si, Mn, Ti, P, Cr, Ni, S, and K. Both natural and synthetic standards were used for calibration. Elemental X-ray maps of both thin sections were obtained for Fe, Mg, Ca, and Si, with an accelerating voltage of 15 kV, a beam current of 25 nA, and a pixel dwell time of 9 ms. Modal abundance of mineral phases was calculated from the resulting X-ray maps using pixel counting techniques within the *ImageJ* software.

2.1.2 Melt inclusion analyses

Olivine hosted polymineralic melt inclusions in both poikilitic and non-poikilitic textures were analyzed in order to calculate the primary trapped liquid composition. Six melt inclusions were analyzed in both thin sections of NWA 10169. Prior to EMP analyses, backscatter electron (BSE) images and qualitative electron-dispersive spectral (EDS) analyses of each melt inclusion were taken on the *JEOL JSM-5610* scanning electron microscope at UNLV. Elemental X-ray maps of P, Cr, and Al within the host olivine were taken using the *JEOL JXA-8200* Suberprobe at

Rutgers University with an accelerating voltage of 15 kV, beam current of 300 nA, pixel dwell time of 500 ms, and a step size of 2 µm. Phosphorus kα was measured on three spectrometers simultaneously [a PET, a TAP, and a large PET (LPET) crystal]. At the ARES laboratory of the Johnson Space Center (JSC), using a *JEOL 8530F* field emission electron probe, elemental X-ray maps of Fe, Mg, Ca, Si, Ti, Al, Cr, K, Na, O, P, Mn, S, and Cl were measured for each of the melt inclusions with an accelerating voltage of 15 kV, a current of 20 nA, and a take-off angle of 34.1°. WDS analyses of major and minor elements were taken for the pyroxene, high-Si mesostasis, and Fe-Ti-Cr oxides within the melt inclusions, as well as the surrounding host olivine. The phosphates, ilmenite and sulfides present were too small (<1 µm) to obtain reliable analyses. These analyses were conducted on the *JEOL JXA-8900* EMP at UNLV, with an accelerating voltage of 15 kV, a beam current of 10 nA (20 nA for host olivine), a spot size of 1 µm (2 µm for host olivine), and standard PAP corrections. Peak count times were 30 s for all elements measured, excluding Na (10 s).

2.2 Quantitative textural analyses

Crystal size distribution (CSD) analyses were performed on the olivine of slide 2. CSDs are conventionally displayed as a plot of ln(population density) vs. crystal size showing a negative log-linear relationship between the two values (e.g., Cashman and Marsh, 1988; Marsh, 1988; Higgins, 2006). The slope of this line = m, and can be defined as $m = -1/G\tau$, where G is the growth rate, and τ is the magma residence time, while the population density (n) can be defined as $n = n_0 e^{(-L/G\tau)}$, where n_0 is the final nucleation density, and L is the crystal size (Marsh, 1998). Using elemental X-ray maps; mosaic maps in plane polarized light (PPL), cross polarized light (XPL), and reflected light; and a petrographic microscope; 506 olivine crystals within NWA 10169 were

traced along their grain boundaries in *Adobe Illustrator*. The minimum number of olivine crystals required to obtain statistically significant results was determined to be 250 grains, for acicular habit (Morgan and Jerram, 2006). Three axes (long, short, and intermediate) were measured on each olivine grain using the *ImageJ* software. All olivine grains with long axes <0.03 mm were left out of future calculations, as they may not represent the true grain size, but rather a projection. The software CSD*slice* (Morgan and Jerram, 2006) was used to take these axes measurements and convert them into three-dimensional true grain size ratios. With the software CSD*correction* (Higgins, 2000), the 3D grain size ratios were used to generate a CSD plot of population density versus crystal size. Using the slope of the generated CSD plot, and an estimated olivine growth rate of 3.1×10^{-8} mm/s, I calculated the average magma residence time for the olivine of NWA 10169.

2.3 Laser Ablation – Inductively Coupled Plasma – Mass Spectrometry (LA-ICP-MS)

In situ trace element compositions of the major phases of NWA 10169 were analyzed using the *New Wave Research UP213* (213nm) solid-state laser ablation system coupled to a *ThermoScientific iCAP Q* ICP-MS at the Scripps Institute of Oceanography (SIO) at the University of California, San Diego (UCSD). Low-Ca pyroxene, high-Ca pyroxene, olivine, maskelynite, and merrillite were measured using a 100 µm laser spot size for the silicate analyses and 50 µm for merrillite analyses. The laser ablated material in a helium atmosphere, and ablated material was subsequently transported to the ICP-MS with an argon carrier gas. The laser was maintained at a frequency of 5 Hz, and a fluence of ~ 3 J/cm^2 throughout all analyses. The measurements were performed with a background measurement time of 20 s, an ablation time of 40 s, and a washout time of 120 s. NIST 610, BHVO-2g, and BCR-2g were used as reference standards, and the order

of points analyzed were as follows: 6 standard points (2 for each standard), 8 unknowns (NWA 10169), and 6 additional standard points. Blanks were measured during the laser warm-up time. Data reduction was performed using an Excel spreadsheet developed by Dr. J. Day.

2.4 Inductively Coupled Plasma – Mass Spectrometry (ICP-MS)

0.5 g chip of bulk NWA 10169 was crushed in an agate mortar used exclusively for martian meteorites. The powder was sent to the Scripps Isotope Geochemistry Laboratory (SIGL) and was digested (along with standards BHVO-2, AGV-1, and BCR-2) in 4 mL of concentrated HF and 1 mL of concentrated HNO_3 for over 72 hours at approximately 150 ºC. The NWA 10169 solution and the standards were analyzed for bulk major, minor and trace element compositions, using a *ThermoScientific iCAP Q* ICP-MS, used exclusively for analyses of solutions, at SIGL. The analyses were standardized against BHVO-2. This analytical technique follows the procedure outlined in Day et al. (2015).

2.5 ^{176}Lu/^{177}Hf isotopic analyses

A separate 1 g bulk sample of NWA 10169 was crushed in an agate mortar used exclusively on martian meteorites. The resulting powder was sieved into >100 µm, 75 – 100 µm, 45 – 75 µm, and <45 µm size fractions. Pyroxene and maskelynite cuts were hand-picked from the >100 µm size fraction. Maskelynite was also separated from the 75 – 100 µm size fraction using lithium metatungstate (~ 2.75 g/cc). Fe-Cr-Ti oxides were isolated from both >100 µm and 75 - 100 µm size fractions using thallium malonate (~ 4.36 g/cc). For both heavy liquid separations, powder and liquid were added to a 15 mL conical test tube and spun in a centrifuge at 2500 rpm for 30 minutes. The heavy separate at the bottom of the test tube was frozen with liquid nitrogen and the

light fraction was poured off. The separates were rinsed 10 times with pure water, and washed in pure water, in an ultrasonic bath for four 15-minute sessions. The final aliquots, S1 (100 mg <45 µm bulk), S2 (100 mg >100 µm bulk minus mineral separates), S3 (100 mg pyroxene), S4 (15 mg maskelynite rich), and S5 (<1 mg Fe-Cr-Ti oxides), were taken to the University of Houston, where they were spiked with a dilute ^{176}Lu-^{178}Hf tracer and partially dissolved in 4 mL of concentrated HF and 0.5 mL concentrated HNO_3 at 110°C for 24 hours. The standards BHVO-2, BCR-2, BIR-1, and a blank, underwent the same procedures as S1-5. The samples were dried down, and digested through microwave digestion in 2 mL concentrated HNO_3, 1 mL concentrated HF, and 1 mL 8M HCl. The samples were then dried down and dissolved once in 8M HNO_3, and twice more in 8M HCl. To isolate Lu and Hf, a 4-stage chemical separation, following the procedures of Münker et al. (2001), was performed on the samples, blank, and standards. The ^{176}Lu/^{177}Hf and ^{176}Hf/^{177}Hf isotope ratios were analyzed using the Nu Instruments NuPlasma II MC-ICP-MS at the University of Houston, following the spike subtraction and internal fractionation correction procedures of Lapen et al. (2004). Analyses of Hf standards, blanks, and aliquots were performed at 40 ppb (15 ppb for S3, S4, S5), and introduced to the ICP-MS through an Aridus II desolvating nebulizer fitted with a 50 µl/min self-aspirating nebulizer. Analyses of UH JMC 475 Hf were performed, bracketing each analysis of unknown, to correct for instrument fractionation. Additionally, analyses of UWisconson-USGS JMC 475 Hf and UH AMES Hf were performed to monitor data quality. The average measured ^{176}Hf/^{177}Hf ratios for UW-USGS JMC-475 Hf, UH AMES Hf, BHVO-2, BCR-2, and BIR-1 standards are 0.282160 ± 64 (n = 6), 0.282362 ± 60 (n = 6), 0.283099 ± 89 (n = 6), 0.282871 ± 108 (n = 3), and 0.283239 (n = 1), respectively (all errors are 2σ). Analyses of Lu standards, blanks and aliquots were performed using the methods outlined Lapen et al.

(2004) and Vervoort et al. (2004). External reproducibility for ^{176}Lu/^{177}Hf and ^{176}Hf/^{177}Hf ratios are 0.2% and 0.005%, respectively.

3. RESULTS

3.1 Petrography

Both thin sections of NWA 10169 exhibit distinct bimodal textures, comprised of poikilitic textures and interstitial non-poikilitic textures (Fig. 1). The poikilitic texture is characterized by pyroxene oikocrysts that both fully and partially enclose olivine and chromite chadacrysts. The terms oikocryst and chadacryst are textural terms that describe a large mineral (oikocryst) that encloses smaller minerals (chadacrysts) within its structure. The pyroxene oikocrysts are anhedral, and significantly larger than any other minerals in the meteorite, at up to 4 mm in diameter. The pyroxene oikocrysts have low-Ca cores, and display a sharp compositional boundary to approximately 500 µm thick high-Ca pyroxene rims (Fig. 2). Olivine chadacrysts range in diameter from 100 to 800 µm, and are rounded and anhedral (Fig. 3). Rare olivine chadacrysts contain polymineralic melt inclusions, ranging in diameter from <100 µm to >400 µm comprised of low and high-Ca pyroxene, Si-rich mesostasis, sulfides, Fe-Cr-Ti oxides, ilmenite, and phosphates (Fig. 4). Chromite chadacrysts are anhedral to subhedral and range from 25 to 100 µm in diameter.

The non-poikilitic texture is interstitial to the large pyroxene oikocrysts. Rather than having low-Ca cores and high-Ca rims, pyroxene in the non-poikilitic zones have a less regular distribution of low-Ca and high-Ca pyroxene. Non-poikilitic pyroxene are subhedral and approximately 500 to 1000 µm in length. Olivine within the non-poikilitic texture are generally larger in diameter than the olivine chadacrysts, approximately 800 µm, but as large as 3 mm in length. Non-poikilitic olivine are subhedral to anhedral, and relative to the olivine chadacrysts, enclose abundant polymineralic melt inclusions. These melt inclusions are similar in size, texture, and mineralogy to those observed within the olivine chadacrysts, and are discussed further in

11

section 3.4. Non-poikilitic spinel are generally partially or fully enclosed by olivine, anhedral to subhedral, and are slightly larger than the chromite chadacrysts at up to 300 µm in diameter. Plagioclase within the non-poikilitic textures are 500 to 1000 µm in diameter, and have been completely shocked into amorphous maskelynite. Pyrrhotite and ilmenite are fine grained (<100 µm) and are generally skeletal. Phosphates within NWA 10169 are majority merrillite with minor apatite. They exist solely within the non-poikilitic zones and are generally fine grained (~ 100-200 µm) elongate crystal laths, however there are a small number of larger (~ 400 µm), more robust crystals.

In addition to the plagioclase being completely converted to maskelynite glass through shock, olivine within both thin sections of NWA 10169 are rusty red/brown, having been darkened through shock, with some crystals darkened to near-opaque (Takenouchi et al., 2017). Located within the non-poikilitic texture of thin section 1, I have observed one shock melt pocket >400 µm in size, with abundant rounded <1 µm oxide and sulfide inclusions (Fig. 3b).

Modal abundances of mineral phases were calculated from Fe, Mg, Ca, and Si X-ray maps of both thin sections of NWA 10169 using the software *ImageJ*. The estimated areal modal abundance, assumed to be equal to volume %, is as follows: 37 mod.% olivine, 34 mod.% pigeonite (low-Ca pyroxene), 12 mod.% augite (high-Ca pyroxene), 15 mod.% maskelynite, 2 mod.% Fe-Cr-Ti oxides, and trace amounts of phosphates, pyrrhotite, and ilmenite.

3.2 Major, minor and trace element mineral composition

3.2.1 Pyroxene

The pyroxene oikocrysts of the poikilitic textures have average core compositions of Wo_{6}-$En_{68}Fs_{26}$, becoming progressively more calcium-rich ($Wo_{7-15}En_{60-67}Fs_{24-26}$) with increasing

distance from the oikocryst cores (Fig. 5 and Table 1). The rims of the pyroxene oikocrysts have an average composition of $Wo_{35}En_{45}Fs_{18}$, marking a sharp compositional boundary between the pigeonite cores and augite rims (Figs. 2 and 5, and Table 1). Pyroxene within the non-poikilitic textures, interstitial to the pyroxene oikocrysts, have compositions ranging from pigeonite ($Wo_{10}En_{58}Fs_{31}$) to augite ($Wo_{33}En_{47}Fs_{20}$) (Fig. 5 and Table 1). Non-poikilitic pyroxene does not exhibit the sharp transition between low-Ca cores and high-Ca rims like the pyroxene oikocrysts, but instead shows a patchy, random distribution of pigeonite and augite (Fig. 2). Representative analyses of pyroxene are listed in Table 1. These compositions, and distributions of pigeonite and augite, are akin to those observed in the enriched poikilitic shergottites RBT 04261/2, NWA 7397, NWA 7755, and Grove Mountain (GRV) 020090 (Usui et al., 2010; Jiang and Hsu, 2012; Howarth et al., 2014; Howarth et al., 2015). The geochemically intermediate poikilitic shergottites (e.g., GRV 99027, Lewis Cliffs – LEW – 88516, and NWA 1950) generally have pyroxene with higher enstatite contents than NWA 10169 (Fig. 5) (e.g., Harvey et al., 1993; Hsu et al., 2004; Mikouchi, 2005). The Mg#s [molar $100*Mg/(Mg+Fe)$] of pyroxene oikocrysts are higher (>70) than those of the non-poikilitic pigeonite (<67). A similar relationship is observed between the high-Ca oikocryst rims and non-poikilitic augite, albeit with greater degrees of overlap (Fig. 6a). Within the poikilitic pigeonite, as Mg# decreases, TiO_2 and Al_2O_3 increase, while Cr_2O_3 shows no relationship. Within the non-poikilitic pigeonite, TiO_2 continues to increase, while Al_2O_3 and Cr_2O_3 begin to decrease with decreasing Mg#. Augite within NWA 10169, as Mg# decreases, show decreasing Cr_2O_3, increasing TiO_2, and no significant relationship with Al_2O_3 (Fig. 6). These compositional trends have also been observed within RBT 04261/2, GRV 020090, and NWA 7397 (Usui et al., 2010; Jiang and Hsu, 2012; Howarth et al., 2014).

The trace elements Y and Zr have positive correlations with Ti in NWA 10169 pyroxene, while Li has a slight negative correlation with Ti in NWA 10169 pigeonite and no relationship in the augite (Fig. 7). The trace element contents vary between the poikilitic and non-poikilitic textures, with Li concentrations slightly decreasing, and Ti, Y, and Zr showing higher abundances in non-poikilitic pyroxene compared to poikilitic pyroxene, displaying an expected increase in incompatible elements across the textures (Fig. 7). As observed with major element trends, there is also a greater degree of overlap between the poikilitic and non-poikilitic augite than pigeonite. The Ti/Al ratios of NWA 10169 pyroxene are relatively uniform within the pyroxene oikocrysts, however Ti increases with decreasing Al in non-poikilitic pyroxene (Fig. 7). The pyroxene in enriched poikilitic shergottite NWA 7397 also shows these same trace element trends (Howarth et al., 2014).

Pyroxene REE contents in NWA 10169 show LREE-depleted profiles, with the greatest degree of LREE-depletion seen in the cores of pyroxene oikocrysts [$(La/Yb)_{CI} = 0.06$]. Pigeonite within the non-poikilitic textures have higher overall REE abundances than the pyroxene oikocrysts, and similar degrees of LREE-depletion [$(La/Yb)_{CI} = 0.07$] (Fig. 8a). Augite of the oikocryst rims, and within the non-poikilitic textures, have overlapping REE profiles with greater abundances of REE, and lower degrees of LREE-depletion [$(La/Yb)_{CI} = 0.10$] than the pigeonite of NWA 10169 (Fig. 8b). The non-poikilitic pyroxene, both pigeonite and augite, have slight negative Eu anomalies of $Eu/Eu^* = Eu_{CI}/(Sm_{CI} * Gd_{CI})^{1/2} = 0.74$ and 0.76, respectively. The REE profiles of pyroxene in NWA 10169 are more LREE-enriched than those of the intermediate poikilitic shergottites (e.g., GRV 99027, LEW 88516), and share affinities with other enriched poikilitic (e.g., RBT 04261/2, NWA 7397), basaltic (e.g., Shergotty, Zagami), and olivine-phyric

14

(e.g., LAR 06319) shergottites (e.g., Harvey et al., 1993; Wadhwa et al., 1994; Hsu et al., 2004; Usui et al., 2010; Balta et al., 2013; Howarth et al., 2014).

3.2.2 Olivine

The most primitive compositions of olivine in NWA 10169 (Fo_{68}) are found in olivine chadacrysts located within the cores of pyroxene oikocrysts, while olivine chadacrysts located closer to the oikocryst rims are progressively more Fe-rich (Fo_{65-61}). The range of compositions observed within the olivine chadacrysts is greater than the observed compositional range within the interstitial, non-poikilitic olivine (Fo_{61-57}) (Fig. 5). Olivine compositions in NWA 10169 are consistent with olivine analyzed within the enriched poikilitic shergottites (e.g., RBT 04261/2, NWA 7397), but are more Fe-rich than those of the intermediate shergottites (e.g., GRV 99027, LEW 88516) (Harvey et al., 1993; Hsu et al., 2004; Usui et al., 2010; Howarth et al., 2014). Representative olivine analyses in NWA 10169 are presented in Table 1. Major element compositions of individual grains of olivine in NWA 10169 are relatively homogenous, with no evidence for continuous major element zonation.

However, olivine shows phosphorus oscillatory zonation, with P_2O_5 contents in olivine are from < 0.05 wt. %, to ~ 0.4 wt.% (Fig. 4). These zonations are preserved (as opposed to Fe and Mg zonations) as phosphorus diffuses very slowly in olivine (e.g., Milman-Barris et al., 2008; Watson et al., 2015) (Fig. 4). In both poikilitic and non-poikilitic zones, the melt inclusions are all surrounded by irregular P-poor regions as also observed in Allen Hills (ALH)A 77005 and Larkman Nunatak (LAR) 06319 (Milman-Barris et al., 2008; Peslier et al., 2010). These P-poor regions often have rounded boundaries, in contrast to the sharp, angular compositional boundaries observed in the more P-rich zoned regions of the olivine (Figs. 4d, 4g, and 4j). I only measured olivine containing melt inclusions near their cores, thus, the true cores of those crystals were not

analyzed. The mapped poikilitic olivine shows a large (~ 150 µm thick) homogeneous, relatively P-poor region surrounded by continuous oscillatory zonings (<10 µm thick) becoming more discontinuous towards the rims. The cores of the non-poikilitic olivine crystals are P-poor and surrounded by euhedral, continuous oscillatory zonings (<10 µm thick) of P-rich and P-poor olivine. Closer to the rims, the P zonation in olivine becomes progressively more discontinuous, with alternating P-rich bands following euhedral crystal shapes that abruptly terminate at the continuous zonation of the interior crystal (Figs. 4d and 4j). These observations are consistent with the P zonation patterns observed in the olivine megacrysts of the enriched olivine-phyric shergottites NWA 1183 and LAR 06319 (Peslier et al., 2010; Shearer et al., 2013). Phosphorus zonations also provide evidence for multiple nucleation sites surrounded by euhedral P-rich growth bands, showing an agglomerated olivine crystals in what appears as single olivine crystal in BSE imagery (Figs. 4d and 4j). Other slow diffusing elements in olivine, such as Al and Cr, do not show any correlation with the P zonings. Additionally, there is no observable spatial correlation between divalent cation contents and P zoning. Olivine crystals of NWA 10169 show evidence of experiencing high degrees of shock, and are highly fractured, leading to the dislocation of high and low-P zonation bands along the trace of the factures.

Trace element concentrations in NWA 10169 olivine are similar in both the olivine chadacrysts and non-poikilitic olivine, with no significant trace element trends observed between the two groups of olivine (Table 2).

Olivine within NWA 10169 have LREE-depleted profiles and REE concentrations lower than the cores of the pyroxene oikocrysts; low enough that LREE concentrations in olivine are often below the detection limit of the LA-ICP-MS (~ 0.003 ppm) (Table 2).

3.2.3 Maskelynite

The plagioclase of NWA 10169 occurs exclusively interstitial to the pyroxene oikocrysts within the non-poikilitic textural zones and have been completely metamorphosed to amorphous maskelynite through shock. Representative analyses of NWA 10169 maskelynite are presented in Table 3. The compositions of maskelynite range from An_{34} to An_{56} with an average of An_{49}, with no evidence for regular compositional zoning (Fig. 9). The majority of maskelynite is K-poor, with an average composition of Or_3, increasing from Or_2 to Or_6 with decreasing An content. The most K-rich maskelynite present is Or_{13}, located near a late-stage phosphate grain (Fig. 9). These compositions are comparable to those observed in the enriched poikilitic shergottite RBT 04261/2, though with lower Ab and Or contents seen in NWA 10169 maskelynite (Usui et al., 2010). The REE contents of maskelynite in NWA 10169 yield LREE-enriched profiles [$(La/Yb)_{CI} = 1.18$], with HREE concentrations often below the detection limit of the LA-ICP-MS (Table 2 and Fig. 8c). The average REE profile for maskelynite shows a positive Eu anomaly [$Eu/Eu* = 14$]; less than the anomalies observed in the enriched shergottites RBT 04261/2, Shergotty, and Zagami (~ 33, ~ 40, ~ 35, respectively) (Usui et al., 2010; Wadhwa et al., 1994).

3.2.4 Fe-Cr-Ti oxides

The Fe-Cr-Ti oxides of NWA 10169 transition from more Cr-rich oxides (chromite) within the pyroxene oikocrysts, to more Ti-rich oxides (ulvöspinel) within the interstitial non-poikilitic textures. Representative analyses of poikilitic and non-poikilitic Fe-Cr-Ti oxides are presented in Table 3 and Figure 10. The chromite chadacrysts within pyroxene oikocrysts and olivine chadacrysts show substitution between chromite and spinel, ranging from Chr_{59} (chromite) Mgn_7 (magnetite) Spn_{21} (spinel) Ulv_{13} (ulvöspinel) to $Chr_{80}Mgn_3Spn_{12}Ulv_4$. One chadacryst located near the rim of a pyroxene oikocryst yielded a composition of $Chr_{33}Mgn_{10}Spn_{10}Ulv_{47}$. The Fe-Cr-Ti oxides interstitial to the pyroxene oikocrysts, within the non-poikilitic texture instead show

evidence for a chromite to ulvöspinel substitution, with compositions ranging from $Chr_{42}Mgn_{10}Spn_{11}Ulv_{37}$ to $Chr_{16}Mgn_{14}Spn_5Ulv_{66}$ (Fig. 10). This transition from chromite-spinel substitution in the poikilitic texture to chromite-ulvöspinel substitution in the non-poikilitic texture is also observed within the enriched poikilitic shergottites RBT 04261/2 and NWA 7397, and the intermediate poikilitic shergottite NWA 4797; though Ti contents in the non-poikilitic ulvöspinel of the enriched poikilitic shergottites are significantly higher than those in the geochemically intermediate NWA 4797 (Usui et al., 2010; Walton et al., 2012; Howarth et al., 2014) (Fig. 10).

3.2.5 Phosphates

Phosphates of NWA 10169 are solely located within the non-poikilitic textures and are predominantly merrillite, an anhydrous Mg-rich Ca phosphate with 45 wt.% P_2O_5, 46 wt.% CaO, 3 wt.% MgO, 2 wt.% Na_2O, and 1 wt.% FeO. The merrillite grains are homogeneous and are identical in composition to those in NWA 7397 (Howarth et al. 2014). Merrillite analyses are summarized in Table 3. Less abundant than merrillite, apatite is present, mainly located within olivine-hosted polymineralic melt inclusions. The diameters of the apatite crystals are commonly < 1 µm, below the size that can be reliably analyzed with an electron microprobe. The apatite is hydrated with F and Cl, with less Mg and Fe than the merrillite.

Compared to the other minerals of NWA 10169, merrillite is enriched in REE with La ~ 555xCI. The average REE profile of merrillite in NWA 10169 is LREE enriched [$(La/Yb)_{CI}$ = 1.45] with a slight negative Eu anomaly [Eu/Eu* = 0.78] (Fig. 8d). Additionally, merrillite in NWA 10169 shows lower overall REE enrichment than those of the other enriched poikilitic shergottites.

3.3 Crystal size distribution

The results of the CSD analyses performed on 506 olivine grains of NWA 10169 are summarized in Table 4 and the CSD profiles of both length and width are shown in Figure 11. The best fit 3D crystal habit for olivine of NWA 10169, calculated by *CSDslice,* is 1.00:1.25:1.90 (rectangular prism) with an R^2 value of 0.90. The slope of the ln(population density) versus crystal size CSD profile is -3.55 and -4.79 for length and width axes, respectively. The y-intercept values for length and width axes are 3.91 and 4.69, respectively. Residence times of olivine in NWA 10169 were calculated using the estimated growth rate of ~ $3.1x10^{-8}$ mm/s of olivine in LAR 06319 (Basu Sarbadhikari et al., 2009); the results for the length and width slopes are 105 days and 78 days, respectively. Both CSD profiles show a negative log-linear slope, with a concave up shape (Fig. 11). Slope flattening occurs for grain sizes larger than ~ 1.2 mm (Fig. 11). A sharp reversal of slope is seen at crystal sizes < 0.2 mm, a feature commonly observed in CSD profiles of igneous rocks (e.g., Marsh, 1988; Higgins, 2006).

3.4 Olivine-hosted polymineralic melt inclusions

Both the olivine chadacrysts of the poikilitic texture, and the interstitial olivine of the non-poikilitic texture, are host to abundant melt inclusions, with a greater proportion being hosted by non-poikilitic olivine (Fig. 4). Melt inclusions represent parent melt trapped within a growing olivine at a specific point of its crystallization history. The presence of such melt inclusions is common within the poikilitic and olivine-phyric shergottites (e.g., Ikeda, 1998; Taylor et al., 2002; Peslier et al., 2010; He et al., 2014; Howarth et al., 2014; Potter et al., 2015; Ferdous et al., 2018). Representative analyses of NWA 10169 melt inclusions and their olivine hosts are presented in the supplementary information; BSE images and X-ray maps of the inclusions can be found in Figure 5. Melt inclusions are present within olivine across the range of present compositions (Fo$_{68}$-

58), thus in both poikilitic and non-poikilitic olivine, and are generally circular to elongate in cross-section. They vary in size from as large as ~ 650 µm to less than 100 µm. The majority of melt inclusions are polymineralic, though there are a number of small (~ 100 µm) homogenous inclusions of Si and Al-rich mesostasis, as well as some melt inclusions that are nearly monomineralic (commonly high-Ca pyroxene). The polymineralic melt inclusions show a relatively concentric succession of minerals from the rim to core of the melt inclusions. The edges of the melt inclusions trapped in more primitive olivine (Fo_{69-65}) have thin (<5 µm) rims of low-Ca pyroxene of compositions $Wo_2En_{68}Fs_{30}$ to $Wo_4En_{65}Fs_{31}$, with a sharp compositional boundary to high-Ca rims ($Wo_{43}En_{41}Fs_{16} - Wo_{46}En_{38}Fs_{16}$) towards the interior of the inclusion. Melt inclusions within the more evolved, non-poikilitic olivine ($Fo_{<63}$) show a similar relationship, though occasionally, the low-Ca pyroxene rim is absent. The rims of high-Ca pyroxene in these inclusions have compositions of $Wo_{44}En_{35}Fs_{21}$ to $Wo_{52}En_{31}Fs_{18}$. Both low-Ca and High Ca pyroxene are present as discrete subhedral to anhedral grains within the interior of the inclusions and are rich in aluminum (up to 12 wt.%). Occasionally at the edges of the inclusions, small troilite (< 10 µm) grains, and large (> 20 µm) Fe-Cr-Ti rich oxides are observed. Their compositions trend from chromite to ülvospinel with decreasing Fo content of the host olivine (Fig. 4). The major phase within the interior of the melt inclusions is Si-Al-Ca rich mesostasis (glass), with feldspathic compositions. The glass has average SiO_2 contents of 73 wt.%, Al_2O_3 contents of 17 wt.%, up to 3 wt. % CaO, and up to 1 wt. % FeO. Glasses in inclusions hosted by olivine ($Fo_{<63}$) are enriched in K_2O (up to 4 wt. %). The phase is unstable under the EMP beam and likely experienced some volatile-loss due to shock (e.g., Goodrich, 2003; Basu Sarbadhikari et al., 2011). Blebs of Si-rich (SiO_2 >85 wt.%) glass pockets are observed within the feldspathic glass of the interior (Fig. 4). Devitrification crystals of feldspar exsolved from the glass are occasionally observed, with

compositions of 48 wt.% SiO_2, 34 wt.% Al_2O_3, 16 wt.% CaO, ~ 1 wt.% Na_2O. In addition, skeletal

phosphates (<5 µm) are present within the interior of the melt inclusions. They are too small to

reliably analyze, though EDS analyses often yield F and Cl peaks, suggesting that they are apatite.

Less commonly, Mg peaks are observed, possibly indicating the presence of merrillite. Needles

(<5 µm) of troilite and ilmenite are also present within the interior of the melt inclusions, though

are less abundant than the skeletal phosphates.

3.5 Lu-Hf crystallization age and isotope systematics

The Lu-Hf isotope compositions of the 5 aliquots (S1-S5) analyzed, crystallization age,

isochron initial isotopic composition, and model $^{176}Lu/^{177}Hf$ and $^{147}Sm/^{144}Nd$ source compositions

are presented in Table 5. The $^{176}Lu/^{177}Hf$ versus. $^{176}Hf/^{177}Hf$ 5-point isochron isochron yielded a

crystallization age of 167 ± 31 Ma (2σ, MSWD = 1.4), and a derived initial $^{176}Hf/^{177}Hf$ ratio of

0.282186 ± 0.000011 (Fig. 12). Using the CHUR parameters of Bouvier et al. (2008b), the

calculated initial $\varepsilon Hf_{(CHUR)}$ value is -17.5, consistent with the enriched shergottites (e.g., Bouvier

et al., 2005; Debaille et al., 2008; Shafer et al., 2010). In order to calculate the source $^{176}Lu/^{177}Hf$

and $^{147}Sm/^{144}Nd$ ratios, the methods of Borg et al. (1997; 2003) were used, on the basis of the

following assumptions: a bulk chondritic Mars (for REE and Hf) that formed at 4.567 Ga (T_0); an

age of 4.504 Ga (T_1) for the differentiation of source reservoirs (Borg et al., 2016); and CHUR

parameters of $^{176}Lu/^{177}Hf = 0.0336$, $^{176}Hf/^{177}Hf_{4.567\,Ga} = 0.279825$, λ-$^{176}Lu = 1.865 \times 10^{-11}$ y^{-1},

$^{147}Sm/^{144}Nd = 0.1967$, $^{143}Nd/^{144}Nd_{4.567\,Ga} = 0.506674$, and λ-$^{147}Sm = 6.54 \times 10^{-12}$ y^{-1} (Bouvier et

al., 2008b). The calculation was performed from the isochron-derived initial $^{176}Hf/^{177}Hf$ and

$^{143}Nd/^{144}Nd$ ratios at T_2 (crystallization age). The model source $^{176}Lu/^{177}Hf$ composition is 0.02748

± 0.00037 (2σ), within the range for other modeled enriched shergottite source compositions,

21

0.02718 ± 0.00027 to 0.02813 ± 0.00027. The source ^{176}Lu/^{177}Hf composition of NWA 10169 is identical within error with the modeled source compositions of other enriched poikilitic shergottites, such as NWA 4468 and RBT 04262; enriched basaltic shergottites Shergotty and Zagami; and enriched olivine-phyric shergottite LAR 06319 (Bouvier et al., 2005; 2008a; Lapen et al., 2008; 2009; Shafer et al., 2010).

4. DISCUSSION

4.1 Crystallization sequence of NWA 10169

The significant differences in mineralogy and mineral major and trace element composition observed across the bimodal texture of NWA 10169 provide the basis of the following interpretations regarding the crystallization history of the meteorite. The olivine chadacrysts and pyroxene oikocrysts of the poikilitic texture have higher Mg#'s than the olivine and pyroxene of the interstitial poikilitic texture, suggesting that the minerals of the poikilitic texture crystallized from a more primitive melt at the early stages of crystallization, as also implied by their texture (Fig. 5). The low-Ca pyroxene oikocrysts also have lower incompatible element abundances, and are more LREE-depleted than the pyroxene of the non-poikilitic texture, further supporting the interpretation that the pyroxene oikocrysts crystallized at an earlier stage than the non-poikilitic texture (Figs. 7 and 8a). Within the poikilitic texture, olivine and chromite chadacrysts are enclosed by the pyroxene oikocrysts, while the chromite chadacrysts are often enclosed by olivine, suggesting initial crystallization of chromite, with a degree of overlap with the initiation of olivine crystallization (Fig. 2). The olivine chadacrysts of NWA 10169 are anhedral with rounded edges, consistent with resorption through reaction with the parent melt (olivine + melt = pyroxene), a reaction suggested to have occurred in the other enriched poikilitic shergottites, RBT 04262 and NWA 7397 (Bard et al., 1986; Usui et al., 2010; Howarth et al., 2014). Following the crystallization of olivine chadacrysts, and subsequent reaction with the melt, the pigeonite cores of the pyroxene oikocrysts crystallized, enclosing the olivine and chromite. The olivine chadacrysts enclosed within the augite rims of the pyroxene oikocrysts have lower Mg#'s than those enclosed in the oikocryst cores, suggesting oikocryst rim crystallization from a more evolved

melt. The rims of the oikocrysts and the augite of the non-poikilitic texture likely co-crystallized, as their incompatible trace element compositions and REE profiles overlap (Figs. 7 and 8b). The slight negative Eu anomaly observed in the poikilitic and non-poikilitic augite REE profiles suggests some co-crystallization with (and possible removal of) plagioclase (Fig. 8e). At the final stages of oikocryst crystallization, the more evolved melt interstitial to the pyroxene oikocrysts begins to co-crystallize pyroxene and olivine with lower Mg#'s than their poikilitic counterparts. Plagioclase co-crystallization at this stage is supported by the shift from increasing Al_2O_3 with decreasing Mg# and Ti in the pyroxene oikocrysts, to decreasing Al_2O_3 with decreasing Mg# in the non-poikilitic pyroxene (Fig. 6d). Crystallization of ülvospinel also began at this stage, marked by the shift from chromite – spinel substitution in the poikilitic Fe-Cr-Ti oxides, to chromite ülvospinel substitution in the non-poikilitic Fe-Cr-Ti oxides (Fig. 10). This shift in compositional trends is consistent with the ülvospinel of the non-poikilitic texture crystallizing after the initiation of plagioclase growth, which removes Al_2O_3 from the melt. The large (>1 mm) grains of olivine (Fig. 3) present within NWA 10169, though they share similar compositions with other non-poikilitic olivine, likely nucleated with the poikilitic olivine; but as they were never trapped by the pyroxene oikocrysts, thus isolated from the melt, they continued to grow and equilibrate with the evolving magma, inheriting the lower Mg#'s of the non-poikilitic olivine. As the interstitial melt continues to crystallize, pockets of highly fractionated melt are isolated and late stage phases such as merrillite, apatite, sulfides, and ilmenite crystallize. The negative Eu anomaly observed in the REE profiles of merrillites support phosphate crystallization following the initiation of plagioclase growth. To summarize, the apparent crystallization sequence of NWA 10169 follows chromite chadacrysts ≥ olivine chadacrysts ≥ oikocryst cores > augite oikocryst rims ≥ interstitial plagioclase, ülvospinel, olivine, and pyroxene > phosphates, sulfides and ilmenite. Similar

crystallization sequences have been proposed for other members of the enriched poikilitic shergottites (Usui et al., 2010; Howarth et al., 2014; Howarth et al., 2015).

4.2 Olivine growth in NWA 10169

Zonation of phosphorus in olivine is commonly observed in igneous rocks, and it has been used to provide insight into olivine crystallization growth in shergottites (Milman-Barris et al., 2008; Peslier et al., 2010; Shearer et al., 2013) and other martian and ordinary chondrite samples (e.g., Goodrich et al., 2013; Balta et al., 2016; McCanta et al., 2016). Phosphorus zonations, unlike major element zonations, are preserved within the olivine of NWA 10169, because phosphorus is highly resistant to diffusion within the olivine structure (Milman-Barris et al., 2008; Watson et al., 2015). Milman-Barris et al. (2008) interpreted P zonation in olivine to have arisen through rapid growth rates leading to disequilibrium conditions, in which the equilibrium partition coefficient for P (<0.1) is elevated, as P is progressively enriched at the growing olivine edge, and subsequently trapped within the crystal. This zonation may manifest either from internal oscillatory growth, or less commonly, as a response to external changes in magma conditions (Milman-Barris et al., 2008). In the olivine of NWA 10169, rounded zones of low-P olivine surround melt inclusions and terminate intersecting P zonations (Fig. 4d, 4g, and 4j). This relationship is also observed in the poikilitic shergottite ALHA 77005, and the olivine phyric shergottite LAR 06319, and has been interpreted to represent slow olivine crystallization from the trapped melt inclusion along the wall of the host olivine (Milman-Barris et al., 2008; Peslier et al., 2010). In the mapped poikilitic olivine (Fig. 4d), a rounded P-poor core, surrounding a melt inclusion, transitions sharply into a relatively homogenous higher-P mantle, suggesting slow, equilibrium crystallization at constant growth rates. Towards the rim of the poikilitic olivine,

continuous oscillatory zonation from P-poor to P-rich olivine is observed, likely the result of an increase in cooling rates, thus faster growth rates, consistent with growth during transport towards the surface (Milman-Barris et al., 2008). Closer to the rim, P-zonation is more discontinuous, consistent with variable growth rates across the surface of a crystallizing olivine, likely in a static magmatic environment, and possibly the result of entrapment in the surrounding pyroxene oikocryst (Shearer et al., 2013). The two mapped non-poikilitic olivine (Fig. 4g and 4j) both show P-poor cores that transition into continuous thin (<5 µm) oscillatory P zonations consistent with rapid crystallization, likely during transport towards the surface (Milman-Barris et al., 2008). The non-poikilitic olivine in figure 4j, like the poikilitic olivine, shows discontinuous P zonation towards its rim, likely representing varying growth rates across the crystal in a highly crystalline, static magma following emplacement (Shearer et al., 2013). The P-poor cores and surrounding continuous P zonation observed in the olivine mapped in NWA 10169, though sometimes obscured by melt inclusions, are similar to those observed in the enriched olivine-phyric shergottites NWA 1183 and LAR 06319 (Peslier et al., 2010; Shearer et al., 2013). These olivine crystals have been interpreted to be phenocrystic or antecrystic in origin, as opposed to the xenocrystic olivine of the depleted olivine-phyric shergottite Y980459, containing partially resorbed, anhedral, P-rich cores (Peslier et al., 2010; Shearer et al., 2013). One olivine crystal within NWA 10169, visible in the upper left corner of figure 4j, contains a P-rich core and is consistent with the olivine observed in Y980459, suggesting a possible xenocrystic origin for that crystal (Shearer et al., 2013). More olivine cores are possibly xenocrystic in NWA 10169, however, melt inclusions in the core of olivine crystals obscure this information.

Experimentally produced olivine show evidence for coupled substitutions between Al, Cr, and P, resulting in correlative zonations observed with these elements (Milman-Barris et al., 2008).

However, the diffusion of P in olivine is slower than Cr, which is in turn slower than the diffusion of Al, which often leads to the relaxation and erasing of Al and Cr in natural olivine (Milman-Barris et al., 2008). In ALHA 77005 olivine there is a correlation between Cr and P zonation, but any evidence of Al zonation has been erased, while in NWA 1183 and Y980459, a correlation between Al and P is preserved in the olivine (Milman-Barris et al., 2008; Shearer et al., 2013). Similar to LAR 06319, there is no observable relationship between P and Al, Cr, or divalent cations in the olivine of NWA 10169 (Peslier et al., 2010). The olivine of these meteorites likely had magma residence times of less than a few months, at temperatures high enough to relax Cr and Al zonation in olivine (~1200 °C), allowing for the preservation of P zoning, and the destruction of Cr and Al zoning (Milman-Barris et al., 2008; Watson et al., 2015). In terrestrial mantle xenoliths, Baziotis et al. (2017) noted no relationship between Al and P in olivine, but attributed this to growth rates fast enough to form P zoning, though continue to incorporate Al at equilibrium, based on the preservation Li gradients, a relatively fast diffusing element. This suggests cooling rates on the order of ~10 °C/h (Baziotis et al., 2017). This cooling rate may be applicable for NWA 10169, though I have not collected data from olivine to provide evidence that Li gradients are preserved, thus future work needs to be done before this hypothesis can be tested.

4.3 Conditions of formation

4.3.1 Emplacement of NWA 10169

Crystal size distribution analyses allow for better understanding of cooling and nucleation history of the parent magma of NWA 10169. The CSD profile (population density versus crystal size) for NWA 10169 is concave up, with the slope flattening at olivine diameters of >1.2 mm, indicating an increased magma residence time (Fig. 11). The shallower slope at larger grain sizes

also indicates that there are greater densities of large diameter olivine than continuous single stage olivine growth would predict, suggesting accumulation of large olivine (e.g., Marsh, 1988). Crystal size analyses have been performed on the olivine of the olivine-phyric shergottites, though not the olivine of the poikilitic shergottites. The CSD profile of NWA 10169 olivine is similar to the profiles calculated for the olivine of the olivine-phyric shergottites LAR 06319, Y980459, Sayh al Uhaymir (SaU) 005, Dar al Gani (DaG) 476, and Tissint, in that all of these shergottites share a kinked CSD profile with shallower slopes at larger grain sizes (Goodrich, 2003; Greshake et al., 2004; Basu Sarbadhikari et al., 2009; Ennis and McSween, 2014; Balta et al., 2015). The kinked profiles of these olivine-phyric shergottites have been interpreted to represent a two-stage cooling history, in which the large olivine megacrysts grew and accumulated in a slow cooling environment and were subsequently entrained en route to the surface where a higher cooling rate led to the steady single-stage growth observed for the smaller groundmass olivine (Goodrich, 2003; Greshake et al., 2004; Basu Sarbadhikari et al., 2009; Ennis and McSween, 2014; Balta et al., 2015). The olivine-phyric shergottites Elephant Moraine (EET) 79001A and Dhofar (Dho) 019 do not show a kink in the CSD slope at larger grain sizes, but rather have CSD profiles that suggest continuous single-stage olivine growth (Ennis and McSween, 2014).

The olivine of NWA 10169 is distinct than the olivine of the aforementioned olivine-phyric shergottites, in that much of the NWA 10169 olivine have been enclosed by pyroxene oikocrysts, thus stopping their continued growth and resulting in smaller grain sizes than would likely be otherwise observed. However, much of the largest grains of olivine within NWA 10169 are not enclosed by pyroxene oikocrysts, and as such, are part of the non-poikilitic texture. The CSD profile supports the interpretation that these large olivine grains nucleated during the formation of poikilitic olivine, where they accumulated and failed to be enclosed by the growing pyroxene

oikocrysts. As they were never enclosed, they continued to grow, while the interstitial magma began to crystallize, consistent with their elevated magma residence times. Similar interpretations have been made for the large olivine of RBT 04262 (Usui et al., 2010). Thus, consistent with the observations made for the aforementioned subset of olivine-phyric shergottites, the kinked CSD profile for NWA 10169 olivine suggests a two-stage cooling history in which poikilitic olivine grow, and accumulate at depth, in a slow cooling environment where a portion of the olivine become trapped in growing pyroxene oikocrysts. As the olivine and pyroxene oikocrysts rise towards the surface, the interstitial magma crystallizes in a faster cooling environment, leading to continuous single-stage growth of the non-poikilitic olivine.

When the CSD profiles for the olivine chadacrysts and the non-poikilitic olivine are compared to one another, a major notable difference is that the olivine chadacryst profile yields a smaller y-intercept than the non-poikilitic olivine profile (Fig. 11). The y-intercept value of CSD profiles is proportional to nucleation density (e.g., Higgins, 2011), suggesting that olivine crystallization before/during oikocryst formation had a lower nucleation density than the non-poikilitic olivine. This lends support to the textural evidence that many of the olivine chadacrysts were being actively resorbed through the peritectic reaction (olivine + melt = pyroxene) (Bard et al., 1986).

4.3.2 Temperature, pressure, and oxygen fugacity

To constrain the pressure during the crystallization of NWA 10169, Ti/Al ratios within pyroxene were determined from both the pyroxene oikocrysts, and non-poikilitic pyroxene (Fig. 7d). Pyroxene Ti/Al ratios decrease with increasing pressure; this correlation has been experimentally calibrated on pyroxene of terrestrial hawaiites, and further calibrated for the enriched olivine-phyric shergottite NWA 1068 (Nekvasil et al., 2004; Filiberto et al., 2010). This

relationship between pyroxene Ti/Al ratio and pressure has been used to estimate the pressure of oikocryst formation in the enriched poikilitic shergottite NWA 7397 (Howarth et al., 2014). The Ti/Al ratios of pyroxene oikocrysts within NWA 10169 suggest crystallization at pressures > 9.3 kbar (Fig. 7d). This estimated pressure, and the consistent Ti/Al ratios, suggests that the pyroxene oikocrysts, and their associated chromite and olivine chadacrysts, crystallized at relatively constant pressure, at depths at or near the base of the martian crust (e.g., Wieczorek and Zuber, 2004). As plagioclase crystallization initiated following oikocryst formation, the efficacy of pressure estimation using Ti/Al in non-poikilitic pyroxene is questionable (McSween et al., 1996). However, the subequigranular, finer grained texture of the non-poikilitic regions suggests crystallization under higher cooling rates than the coarse pyroxene oikocrysts, likely at lower pressures nearer to the surface. Additionally, for the poikilitic shergottites Y000027 (and pairs) and RBT 04262, pressures consistent with near surface conditions (~ 1 bar) were estimated (Mikouchi and Kurihara, 2008; Usui et al., 2010). Though possibly affected by plagioclase crystallization, the pyroxene of the non-poikilitic texture show a trend of increasing Ti/Al ratios, with higher ratios consistent with pressures near the martian surface (~ 1 bar), suggesting crystallization of magma interstitial to the pyroxene oikocrysts at dynamic pressures, perhaps while rising from the lower crust towards the surface (Fig. 7d).

To constrain the oxygen fugacity and temperature conditions during various stages of the crystallization of NWA 10169, the olivine-spinel geothermometer and the olivine-pyroxene-spinel oxybarometer were used on mineral assemblages in both the poikilitic and non-poikilitic textures (Sack and Ghiorso 1989, 1991a, 1991b, 1994a, 1994b, 1994c,; Ballhaus et al., 1991; Wood, 1991; http://melts.ofm-research.org/CORBA_CTserver/Olv_Spn_Opx/index.php). In both the poikilitic and non-poikilitic textures, I use low-Ca pyroxene, olivine, and spinel in contact with each other,

and thus in equilibrium. As oxygen fugacity is pressure dependent, the ~ 10 kbar pressure estimate from pyroxene Ti/Al ratios was used for the subsolidus equilibration fO_2 calculations for the poikilitic textures. Pressures of ~ 1 bar were assumed for the non-poikilitic calculations, consistent with assumptions used for calculations of fO_2 within the enriched poikilitic and olivine-phyric shergottites (e.g., Herd, 2003; Usui et al., 2010; Howarth et al., 2014). The subsolidus equilibration temperature estimated for the poikilitic textures is 1065 ± 26 ^{o}C, while the associated fO_2 estimate is 2.30 log units below the fayalite-magnetite-quartz buffer (FMQ -2.30 ± 0.23). The subsolidus equilibration temperature estimated for the non-poikilitic textures is 800 ± 61 ^{o}C, and the associated fO_2 estimate is FMQ -1.07 ± 0.14, over one log unit more oxidizing than the estimate for the early stage poikilitic texture. The only other poikilitic shergottites to have fO_2 estimated for both the poikilitic and non-poikilitic textures are NWA 7397 and NWA 7755 (Howarth et al., 2014, 2015). Additionally, the olivine-phyric shergottites LAR 06319 and Tissint, also had their early and late-stage fO_2 estimated (Basu Sarbadhikari et al., 2009; 2011; Peslier et al., 2010; Balta et al., 2015). The pyroxene oikocrysts of NWA 10169 equilibrated under slightly more reducing conditions than these three meteorites. The early and late-stage fO_2 range of NWA 10169 is consistent with those of NWA 7397 and NWA 7755, yet less than the >2 log unit difference estimated for LAR 06319 (Basu Sarbadhikari et al., 2009; 2011; Peslier et al., 2010; Howarth et al., 2014; 2015). This significant change in fO_2 in LAR 06319 was estimated by Peslier et al. (2010) to have occurred gradually throughout steady crystallization of the meteorite (known as auto-oxidation), based on the idea that Fe^{3+} behaves as a highly incompatible element throughout crystallization. However, stating that Fe^{3+} becomes more compatible as high-Ca pyroxene and oxides begin crystallizing from the melt, Balta et al. (2013) suggested that the ~ 2 log unit difference in fO_2 of LAR 06319 cannot be achieved solely by increasing Fe^{3+} content; but rather,

it requires the addition of an outside O source or degassing of H. Furthermore, Castle and Herd (2017) showed, through thermodynamic MELTS modeling, that fO_2 variation greater than ~ 1 log unit cannot be accounted for solely through auto-oxidation. The differences between estimated early and late-stage fO_2 for the enriched poikilitic shergottites NWA 7397 and NWA 7755 are less distinct (~ 1.3 and 0.7 log units, respectively) than those estimated for LAR 06319, and as such, it has been suggested that these differences can be accounted for through oxidation from continuous crystallization and possible degassing (Howarth et al., 2014; 2015). Thus, the ~ 1.2 log unit difference between poikilitic and non-poikilitic fO_2 of NWA 10169 may be accounted for through auto-oxidation during continuous crystallization, with the possibility for degassing.

A polybaric formation model has been proposed for the enriched poikilitic shergottites, in which the chromite, olivine, and enclosing pyroxene oikocrysts crystallized at depth in a magma staging chamber, followed by the subsequent rise of the parent magma towards the surface and crystallization of the interstitial melt at lower pressure (Howarth et al., 2014). This hypothesis is supported by the dynamic pressures, temperatures, and oxygen fugacities present during the formation of NWA 10169, and indicates a petrogenetic link with the enriched poikilitic shergottite NWA 7397 (Howarth et al., 2014).

4.3.3 Relationship of oxygen fugacity to geochemical sources

The degree of LREE-enrichment of the shergottites, represented by their bulk La/Yb ratio, shows a loose correlation with the oxygen fugacity conditions present upon their respective formations, suggesting that the sources of the geochemically enriched and depleted shergottites are oxidized and reduced, respectively (e.g., Herd et al., 2002; Herd, 2003) (Fig. 13). However, as more shergottites are studied, the correlation between oxygen fugacity and LREE-enrichment becomes fuzzy. A number of the olivine phyric shergottites (Tissint, NWA 6234, NWA 1068, and

LAR 06319) show evidence for a late stage oxidation event, leading to an up to 4 log unit difference between early-stage and late-stage fO$_2$ (Herd, 2006; Peslier et al., 2010; Gross et al., 2013; Castle and Herd, 2017). The early-stage oxygen fugacity of NWA 10169, more reduced than other enriched shergottites, overlaps with the intermediate shergottites (e.g., Goodrich et al., 2003; Herd, 2003; Lin et al., 2005). The enriched gabbroic shergottite, NWA 7320, formed under an oxygen fugacity ~ QFM, but has a low bulk La/Yb ratio (~ 0.55) (Udry et al., 2017). Finally, the geochemically depleted, augite-rich, basaltic shergottite NWA 8159 experienced highly oxidizing conditions (QFM +2) (Herd et al., 2017). This overlap of the oxygen fugacities of the shergottites suggests that the martian mantle is perhaps more heterogeneous than previously thought, with sources of varying oxygen fugacity. Processes such as degassing and crustal contamination through fluids could also explain the large ranges of fO$_2$ within shergottites.

4.4 Geochemical classification and REE budget

Poikilitic shergottites are cumulate rocks, and thus, their measured bulk composition might not be entirely representative of their true compositions. For this reason, I both measured and calculated bulk REE compositions of NWA 10169. The calculated bulk REE composition was inferred using the REE compositions for olivine, pigeonite, augite, maskelynite, and merrillite, and weighting the average according to their respective modal abundances in NWA 10169. Though making up ~ 2% of NWA 10169, Fe-Cr-Ti oxides were not included in the calculation, as their abundances of REE are extremely low, near the detection limit of the LA-ICP-MS. Out of all the phases present within NWA 10169, merrillite is the major carrier of REE (341-555 x CI), and as such, despite its rarity in the rock (< 0.5%), exerts the largest control on the bulk REE composition. A 100% increase in the abundance of merrillite leads to a ~ 90% increase of bulk LREE abundance

and a ~ 40% increase of bulk HREE abundance. In contrast, a 100% increase in the abundance of pigeonite results in only a ~ 2% increase of bulk LREE abundance. The importance of merrillite with regards to bulk REE composition has been recognized within the poikilitic shergottite suite and in shergottites in general (e.g., Hsu et al., 2004; Shearer et al., 2015). The calculated bulk REE profile is shown in Figure 8e, and is compared to the measured bulk REE profile and average profiles for the main mineral constituents of NWA 10169.

The calculated bulk rock REE pattern is consistent with the REE profile of the measured bulk rock REE profile, both relatively flat LREE-enriched profiles with slight positive Eu anomalies [Eu/Eu*$_{CI}$ = 1.14 (meas), 1.32 (calc)] (Fig. 8e). The measured bulk REE profile indicates that NWA 10169 has the highest degree of LREE-enrichment within the shergottite suite, higher than the enriched olivine-phyric shergottite, NWA 1068 (Barrat et al., 2002). However, the measured bulk composition is overall ~ 100% more enriched in REE than the calculated bulk REE compositions of NWA 10169. This can be explained by higher modal content of merrillite in the measured chip than in the thin sections, leading to higher overall REE content. Merrillite, the main carrier of REE in NWA 10169, is solely present within the non-poikilitic textures, so as the relative proportions of interstitial and oikocrystic material change, so too will the overall abundance of merrillite. In addition, the bimodal nature of the poikilitic shergottites makes them inherently heterogeneous with regards to pyroxene oikocryst distribution (e.g., McSween and Treiman, 1998; Bridges and Warren, 2006). The relative proportions of poikilitic to non-poikilitic material represented in the thin sections may be significantly different than that of the bulk rock. This finding stresses the importance of ensuring that poikilitic shergottite samples are as representative of the bulk rock as possible.

In addition, the measured bulk REE profile shows a greater enrichment of La (La/Yb_{CI} = 1.18) than that of the calculated bulk REE profile (La/Yb_{CI} = 0.78) (Fig. 8e). This enrichment may have arisen through hot desert alteration, which has been shown to mobilize and elevate La, Ce, Sr, and Ba contents (e.g., Crozaz et al., 2003). Cracks filled with terrestrial calcite are present within NWA 10169, and suggest that alteration had occurred, though the extent of alteration is not clear. Efforts to avoid these cracks were made during LA-ICP-MS analysis, though there was no way to avoid the cracks while crushing a sample of NWA 10169 for bulk analysis. The bulk composition of NWA 10169 shows enrichments in Sr and Ba, ~ 40 ppm and ~ 300 ppm, respectively, suggesting some degree of terrestrial alteration. Similar enrichments have been observed in the other hot desert enriched poikilitic shergottite NWA 7397 (Howarth et al., 2014).

The measured bulk REE profile of NWA 10169, normalized to CI, is relatively flat and LREE-enriched (La/Yb_{CI} = 1.18), consistent with the REE profiles of the enriched shergottites Zagami, Shergotty, LAR 06319, RBT 04262, NWA 7397, and GRV 0200090 (Lodders et al., 1998; Basu Sarbadhikari et al., 2009; Usui et al., 2010; Jiang and Hsu, 2012; Howarth et al., 2014) (Fig. 14). This La/Yb_{CI} value is higher than any recorded within the shergottite suite (Fig. 13). The REE composition, textural characteristics, and mineral major element compositions of NWA 10169 are consistent with those of the enriched poikilitic shergottites, allow for its classification as the sixth member of this group of meteorites (Figs. 5, 9, 11).

4.5 Parental melt of NWA 10169

The poikilitic shergottites are cumulate rocks, as shown by their texture (e.g., Stolper and McSween, 1979; McSween and Treiman, 1998; Goodrich, 2002; Papike et al., 2009; Filiberto et al., 2010; Filiberto and Dasgupta, 2011). Most shergottites show cumulate components, except a

few notable exceptions (e.g., Y980459, LAR 06319, and NWA 6234) that have been interpreted

to represent near magmatic compositions (e.g., Basu Sarbadhikari et al., 2009; Usui et al., 2010;

Gross et al., 2013). The cumulate signature of NWA 10169 was confirmed by the Fe/Mg values

of the most primitive olivine chadacryst cores, the first phase to crystallize (see section 4.1), plotted

against the bulk Fe/Mg value. This value did not plot on the experimentally determined equilibrium

$K_D^{Fe/Mg}{}_{olivine/melt}$ value of 0.35 ± 0.01 (Filiberto and Dasgupta, 2011). This indicates that the first

olivine to crystallize from the parent magma of NWA 10169 are not in equilibrium, with regards

to Fe-Mg, with the bulk NWA 10169 composition (Filiberto and Dasgupta, 2011). Thus, the bulk

composition of NWA 10169 does not represent a magmatic composition.

      To estimate a parental melt composition, olivine-hosted, polymineralic melt inclusions,

located in the primitive olivine chadacrysts and in the later-stage interstitial olivine, were analyzed

in NWA 10169. Melt inclusions have been used to calculate an estimate parental melt composition

for a number of olivine-phyric shergottites and nakhlites (e.g., Peslier et al., 2010; Goodrich et al.,

2013; Potter et al., 2015; Sonzogni and Treiman, 2015). These melt inclusions represent portions

of trapped melt that have been enclosed by growing olivine crystals at a specific point in time. I

measured six melt inclusions in NWA 10169: One (MI1) trapped in a relatively primitive olivine

chadacryst ($\sim Fo_{66}$), assumed to represent the closest approximation to the parental melt of NWA

10169, and five others (MI5, MI6, MI10, MI15, and MI19) trapped in non-poikilitic olivine ($\sim$

Fo_{63-59}), assumed to represent melt trapped at later stages of parent melt evolution (Table 6). To

ensure that the melt inclusions can yield primary trapped liquid (PTL) compositions that are

representative of the magma composition extant during the trapping of the melt, I followed

methods similar to those outlined by Peslier et al. (2010). To establish that the cross-section of the

melt inclusions exposed on the thin sections do not represent off-center cuts, I have only included

melt inclusions that have late-stage phases (e.g., ilmenite, sulfide, high-Si glass) present in their interiors. In addition, to minimize the risk that the compositions of the trapped melt have been altered since their entrapment, P X-ray maps were measured for three of the host olivine to ensure that no disruptions of P-zonations link the melt inclusions to their host olivine rims (see section 4.2) (Fig. 4).

Following the criterion outlined above, I identified the six melt inclusions of this study and calculated their present bulk composition (PBC) using elemental X-ray maps measured on the *JEOL 8530F* at NASA-JSC and the thermoelectron NSS software. This software enables the digitization of the areal extent of the melt inclusions within the X-ray maps, and subsequent amalgamation of X-ray counts into a single X-ray spectrum for each melt inclusion. The resulting X-ray spectra are then compared to standard X-ray spectra and quantified into bulk compositions through the phi-rho-Z (PRZ) matrix correction routine. The calculated PBC for each melt inclusion is not equivalent to the PTL composition however, as the PBC compositions do not plot along the 0.35 K_D $^{Fe/Mg}$ $_{olivine/melt}$ line (Filiberto and Dasgupta, 2011). This is likely due to the "Fe-loss" process described by Danyushevsky et al. (2000). Following melt entrapment, olivine, indistinguishable from the host olivine, begins to crystallize along the wall of the host olivine, becoming more Fe-rich as crystallization continues. The more Fe-rich olivine, crystallized from the melt inclusion, drives the initiation of re-equilibration between the melt inclusion and the host olivine, in which Fe from the melt inclusion diffuses into the host olivine, and Mg diffuses into the melt inclusion (Danyushevsky et al., 2000). To account for the wall olivine crystallization and the Fe-Mg re-equilibration with the host olivine, I used the PETROLOG3 software with the olivine/melt model of Ford et al. (1983) (Danyushevsky et al., 2002; Danyushevsky and Plechov, 2011). The main assumption of this model is that the host olivine composition has not significantly

changed since melt entrapment, and the algorithm requires the user input of the host olivine forsterite content and the FeO_T content of the melt upon entrapment (FeO*) (Danyushevsky and Plechov, 2011). As the FeO* value is unknown, I performed the calculations using a variety of FeO_T values from the following compositions of meteorites within the enriched shergottite suite: Bulk LAR 06319 (Basu Sarbadhikari et al., 2009), PTL of LAR 06319 melt inclusions in $Fo_{>72}$ olivine (Peslier et al., 2010), bulk RBT 04262 (Anand, 2008), bulk Zagami, and bulk Shergotty (Lodders, 1998). I did not use the bulk composition of NWA 10169 as it does not represent a liquid composition. Once the PTL composition was calculated for the melt inclusion (MI1) trapped within the poikilitic, Fo_{66} olivine, I performed isobaric (1 kbar) fractional crystallization modeling by running the alphaMELTS algorithm (Ghiorso and Sack, 1995; Asimow and Ghiorso, 1998; Smith and Asimow, 2005). I ran the algorithm with an initial temperature of 1600° C to ensure modeling started above the liquidus, and an initial oxygen fugacity of FMQ -2, consistent with values determined through oxybarometry (see section 4.3). Through this method, FeO* values for the melt inclusions trapped within the non-poikilitic Fo_{63-59} olivine were estimated by isolating melt compositions in equilibrium with the respective olivine compositions. Thus, enabling the calculation of the PTL compositions of the remaining melt inclusions.

The PBC and PTL compositions of the six melt inclusions studied within NWA 10169 are presented in Table 6. The presented MI1 PTL composition is calculated using the FeO* value from the bulk Shergotty composition of Lodders (1998), as this value provided results the most consistent with prior melt inclusion studies within the enriched shergottite suite (e.g., Peslier et al., 2010; Basu Sarbadhikari et al., 2011). The calculated PTL compositions of the NWA 10169 melt inclusions show decreasing Mg# with decreasing host olivine forsterite content, indicating that MI1, with a host olivine of Fo_{66}, was likely trapped at the early stages of crystallization; thus, its

PTL composition may be used as a proxy for the parental melt composition of NWA 10169 (Table 6 and Fig. 15). The estimated parent melt of NWA 10169 is similar to the whole rock composition of Shergotty, though with a slightly lower Mg#, and lower Na_2O content (Lodders, 1998). Additionally, it is also similar to the PTL of a melt inclusion trapped within a Fo_{66} olivine megacryst of LAR 06319, though with less K_2O and Na_2O (Peslier, 2010). The trends observed from MI1 to the melt inclusions trapped at later stages of magma evolution are broadly consistent with those observed in the melt inclusions of LAR 06319 (Peslier et al., 2010; Basu Sarbadhikari et al., 2011). Both NWA 10169 and LAR 06319 show constant Al_2O_3 content with decreasing Mg#, indicating melt entrapment before fractionation of plagioclase (Fig. 15). There is a slight increase of SiO_2 observed with decreasing Mg# of melt inclusions in NWA 10169, in contrast with the slight decrease of SiO_2 observed in the melt inclusions of LAR 06319 (Fig. 15). The low SiO_2 contents of MI15 are likely a result of there being a large (>10 µm) Fe-Cr-Ti oxide grain within the melt inclusion that may have been primary (i.e. present prior to melt entrapment) (Table 6). The CaO contents of NWA 10169 melt inclusions decrease with decreasing Mg#, a trend that extends into the trend observed in preliminary MI data for RBT 04262, consistent with fractionation of a Ca-rich phase, likely high-Ca pyroxene in the case of NWA 10169 (Potter et al., 2015) (Fig. 15). Preliminary PTL compositions of melt inclusions within RBT 04262 and NWA 7397 have more evolved Mg#s (as low as ~ 20) than those observed in NWA 10169 and LAR 06319, a relationship suggesting that the melt inclusions within these meteorites may have been trapped at a relatively later stage than those of NWA 10169 and LAR 06319. (Peslier et al., 2010; Basu Sarbadhikari et al., 2011; He and Xiao, 2014; Potter et al., 2015; Ferdous et al., 2018) (Fig. 15). Note that melt inclusion compositions in NWA 7397 measured by He and Xiao (2014) are very close to the more evolved melt inclusions of NWA 10169. The compositional trends observed

in the PTL compositions of NWA 10169 melt inclusions show similar magma evolution with LAR 06319 and potentially RBT 04262.

The K_2O contents of melt inclusions in NWA 10169 are highly variable, and show a dichotomy between K-poor melts (< 0.20 wt.%) and K-rich melts (up to 4 wt.%) (Fig. 15 and Table 6). This dichotomy is also observed in the melt inclusions of LAR 06319 and NWA 7397, where MI15 of NWA 10169 has K_2O contents nearly identical to the K-rich melt of NWA 7397 (Peslier et al., 2010; Basu Sarbadhikari et al., 2011; He and Xiao, 2014) (Fig. 15). Goodrich et al. (2013) observed similar K-rich compositions preserved in melt inclusions in nakhlites, and attributed this to be a result of a metasomatized mantle source, based upon LREE (namely Nd) enrichment (e.g., Treiman, 2003). Goodrich et al. (2013) also noted that these K-enrichments are likely true, and not a result of boundary layer effects, as the magnitude of observed enrichment is too large, and there is no correlation of increasing K-enrichment with decreasing melt inclusion size. These observations hold true for NWA 10169, indicating that the observed K-rich melt inclusions are not the result of boundary layer effects. Further evidence that the observed variation of K_2O is representative of the trapped melt, comes from K X-ray maps of the two most K-enriched melt inclusions (MI5 and MI15) that show ubiquitous homogenous K-Si-Al-rich glass, indicating that the variation did not arise through variable exposure of K-rich phases at the thin section surface. The K-rich melt inclusions MI5 and MI15 have variable K_2O/Na_2O, 14.5 and 1.4, respectively, larger than the value of 2 reported for the nakhlite parent melt (Goodrich et al., 2013). The large K_2O/Na_2O ratio reported for MI5 is likely a result of the volatile loss of Na_2O from the unstable Si-Al rich glass during peak shock pressures (e.g., Goodrich, 2003; Basu Sarbadhikari et al., 2011). Furthermore, the K/Ti ratios of the K-rich melt inclusions of NWA 10169 are consistent with those of the nakhlite parent melt, Gale crater rocks, and some Gusev crater rocks, and are suggestive of

40

metasomatism; meanwhile, the K/Ti ratios of the K-poor melt inclusions, are consistent with igneous fractionation (Treiman and Filiberto, 2015; and Filiberto, 2017). Though the K-rich melt inclusions in the nakhlites suggest sampling of a metasomatized mantle source, the K-rich melt inclusions in NWA 10169, only present in the non-poikilitic olivine, represent evidence for the assimilation of metasomatized, K-rich crustal material following transport towards the surface and initiation of non-poikilitic olivine crystallization; an event that likely also occurred during the formation of NWA 7397 and LAR 06319.

4.6 Shergottite crystallization ages and model Lu-Hf source composition

The crystallization ages of the shergottites, dated using the Lu-Hf, Sm-Nd, and Rb-Sr isotope systems, have a general range of 150 Ma to 574 Ma (e.g., Nyquist et al., 2001; Shafer et al., 2010; Brennecka et al., 2014), with two meteorites, Norwest Africa (NWA) 7635 and NWA 8159, as old as ~ 2.4 Ga, extending shergottite magmatism to the early Amazonian (Herd et al., 2017; Lapen et al., 2017). The 167 ± 31 Ma age measured in this study of NWA 10169 (Fig. 12) is concordant with the ~150 – 225 Ma Lu-Hf, Sm-Nd, and Rb-Sr ages determined for the other enriched shergottites (e.g., NWA 4468, Shergotty, NWA 856, RBT 04262, LAR 03619) (e.g., Nyquist et al., 2001; Borg et al., 2008; Lapen et al., 2009; Shafer et al., 2010; Ferdous et al., 2017). The age of NWA 10169 is also similar to the ~170 – 212 Ma Lu-Hf, Sm-Nd, and Rb-Sr ages of the intermediate shergottites, though younger than the ~327-574 Ma ages of the depleted shergottites (e.g., Nyquist et al., 2001; Shih et al., 2005; Misawa et al., 2006; Shih et al., 2011; Brennecka et al., 2014). Paradoxically, the Pb-Pb ages of shergottites are significantly older (~4.1-4.3 Ga) than the Lu-Hf, Sm-Nd, and Rb-Sr ages, and it has been suggested that younger ages may result of resetting through shock or aqueous alteration (e.g., Borg et al., 1999; Bouvier et al., 2005;

2008a; 2009). Shafer et al. (2010) noted that shock, while perhaps capable of mobilizing Rb, Sr, Lu, Hf, Sm and Nd, would likely only redistribute these elements through a closed system, leaving the bulk isotopic composition undisturbed. Thus, if the younger ages have been reset, the time-integrated bulk isotope ratios of the shergottites, modelled back to >4 Ga, yield unrealistically depleted source values (Shafer et al., 2010). Furthermore, Bloch and Ganguly (2014) showed that, in the enriched poikilitic shergottite RBT 04262, there is no evidence for significant elemental diffusion occurring at peak shock pressures and temperatures, and that it is unlikely that the Lu-Hf and Sm-Nd ages of the shergottites had been reset through shock. Additionally, The U-Pb age (~156 Ma) of pure pyroxene and maskelynite fractions from Zagami, indicate that the whole-rock U-Pb age has been disturbed, possibly by the addition of high $^{207}Pb/^{206}Pb$, produced through alteration of the martian surface (Borg et al., 2005). Since NWA 10169 shows no evidence of aqueous alteration (other than the calcite-filled fractures and Ba-enrichments associated with terrestrial alteration), and has initial $\varepsilon Hf_{(CHUR)}$ and model $^{176}Lu/^{177}Hf$ source values that are consistent with other enriched shergottites, I interpret the Lu-Hf age of 167 ± 31 Ma to represent the true crystallization age (Bouvier et al., 2005; 2008a; Lapen et al., 2008; 2009; Shafer et al., 2010).

The modeled source $^{176}Lu/^{177}Hf$ composition of NWA 10169 is 0.02748 ± 0.00037, and is based upon the source differentiation age of Borg et al. (2016), the CHUR parameters of Bouvier et al. (2008b), and the isochron derived initial $^{176}Hf/^{177}Hf$ of NWA 10169. This modeled source value is identical, within error, to the modeled source values (0.02718 ± 0.00027 to 0.02749 ± 0.00027) of the enriched shergottites LAR 06319, NWA 4468, Shergotty, Zagami, and RBT 04262, indicating a likely shared geochemical source between NWA 10169 and this group of enriched shergottites (Bouvier et al., 2005; 2008a; Lapen et al., 2008; 2009; Shafer et al., 2010)

(Figure 16 and Table 5). The crystallization ages within this group of shergottites spans from 150 $\pm$ 29 Ma to 225 $\pm$ 21 Ma for NWA 4468 and RBT 04262, respectively, with the crystallization age of NWA 10169 falling within this range (Borg et al., 2008; Lapen et al., 2008). The range of crystallization ages indicates that this shared geochemical source was persistent in the interior of Mars for at least 75 Ma. Another group of enriched shergottites, Los Angeles, NWA 856, and NWA 7320, crystallized contemporaneously with the first group, though sampled a different source, with distinct modeled source ^{176}Lu/^{177}Hf compositions (0.02789 $\pm$ 0.00028 to 0.02813 $\pm$ 0.00027) (Nekvasil et al., 2001; Brandon et al., 2004; Debaille et al., 2008; Udry et al., 2017) (Fig. 16). Although ejection age analyses for NWA 10169 were not performed, the similar crystallization age and source compositions of the enriched poikilitic, olivine-phyric, and basaltic shergottites may indicate a similar magmatic system forming the shergottites at the same location on Mars. The source affinities and contemporaneous crystallization ages also suggest a heterogeneous martian mantle, in which there were at least two distinct enriched mantle sources being tapped by the enriched shergottite suite at the time of their formation.

4.7. Petrogenetic model for NWA 10169 and the enriched shergottites

Here I present a petrogenetic model for NWA 10169, from the extraction from its source, to its emplacement. I compare this model with other members of the enriched shergottites. A summary of this petrogenetic model is presented in figure 17. Based on REE contents and the enriched εHf$_i$ of -17.5 of NWA 10169, this rock sampled from a geochemically enriched source. Additionally, NWA 10169 shows the highest bulk La/Yb$_{CI}$ (1.18) value observed within the enriched shergottites, though this elevated value may be due in part to terrestrial hot desert alteration (e.g., Crozaz et al., 2003). The modeled source ^{176}Lu/^{177}Hf composition, as discussed in

section 4.6, indicates the source for NWA 10169 was also tapped by the enriched shergottites Shergotty, Zagami, LAR 06319, NWA 4468, and RBT 04262. Based on poikilitic olivine, low-Ca pyroxene, and spinel assemblages in NWA 10169, the fO_2 of this source is likely at least two log units below the FMQ buffer; a value that overlaps with the intermediate shergottites, and shows that there may not be as strong of a correlation between fO_2 and geochemical source as was previously suggested. Initial crystallization of NWA 10169 (Fig. 13).

After melting of this enriched source, initial crystallization of olivine and chromite chadacrysts, followed by pyroxene oikocrysts, occurred at pressures of ~ 10 kbar in a magma staging chamber near the base of the martian crust (e.g., Wieczorek and Zuber, 2004). Olivine growth rates were relatively slow at this stage based on relatively homogenous P content near in the interior of an olivine chadacryst (Fig. 4d). Melt inclusions trapped in olivine at this stage are assumed to represent an approximation of the parental melt, and the estimated parent melt composition for NWA 10169 is similar to the bulk Shergotty composition and melt inclusions of LAR 06319 (Lodders, 1998; Peslier et al., 2010). Crystal size distribution analyses show that olivine chadacrysts became unstable in the parent melt and began to be resorbed prior to enclosure in the pyroxene oikocrysts.

Following crystallization in a magmatic chamber at depth, oikocrysts were entrained close to the surface, which were likely resorbed during decompression, accounting for their rounded shape, as described by Howarth et al. (2014). During magma ascent and eventual entrainment of oikocrysts near the surface, cooling rates increased while pressure decreased, and the more equigranular non-poikilitic olivine, pyroxene, and plagioclase began to crystallize, along with the augitic oikocryst rims. Non-poikilitic olivine show continuous oscillatory P zonations surrounding P-poor phenocrystic to antecrystic cores, indicative of fast olivine growth in the surrounding melt,

likely during magma ascent; a feature consistent with olivine zonations in the enriched olivine-phyric shergottites LAR 06319 and NWA 1183 (Milman-Barris et al., 2008; Peslier et al., 2010; Shearer et al., 2013). A certain amount of xenocrystic input is possible at this stage, as a non-poikilitic olivine is observed with a P-rich resorbed core. Melt inclusions trapped during this stage show normal magmatic evolution similar to those trapped in LAR 06319, but less evolved than those trapped in RBT 04262 and NWA 7397, indicating that these melts were trapped at a later stage of magma evolution (Peslier et al., 2010; Basu Sarbadhikari et al., 2011; Potter et al., 2015; Ferdous et al., 2018). Potassium-rich melt inclusions in NWA 10169, provide evidence for the assimilation of metasomatized K-rich crustal material at this stage, a process that likely occurred during the formation of NWA 7397 and LAR 06319 as well (Peslier et al., 2010; He and Xiao, 2014).

From the magmatic chamber at depth, to emplacement in the near-surface, auto-oxidation and possible degassing contributed to a more oxidizing environment, in the NWA 10169 parental magma, with an fO$_2$ of around one log unit below the FMQ buffer. Upon emplacement at hypabyssal depths, late stage merrillite, ilmenite, and sulfides crystallize, and the rims of olivine show discontinuous oscillatory P zonations, consistent with growth in a highly crystalline, static magmatic environment (e.g., Shearer et al., 2013). This three-stage, polybaric, petrogenetic model for the formation of NWA 10169 is likely ubiquitous amongst the enriched poikilitic shergottites, and a similar polybaric crystallization model has been proposed by Howarth et al. (2014) for NWA 7397.

The crystallization age for NWA 10169 is 167 ± 31, falling within the range of the enriched shergottites Shergotty, Zagami, LAR 06319, NWA 4468, and RBT 04262 (~ 150 Ma to ~ 225 Ma) (e.g., Nyquist et al., 2001; Borg et al., 2008; Lapen et al., 2008). These meteorites also have

identical model ^{176}Lu/^{177}Hf source compositions to NWA 10169. Thus, a long-lived (at least 75 My) magmatic system, originating from the same source, existed on Mars and is likely responsible for the formation of this group of shergottites. This links shergottites with different textures (e.g., poikilitic, olivine-phyric, basaltic) to the same long-lived magmatic system, whilst also suggesting that though the intermediate and enriched poikilitic shergottites were likely emplaced in a similar manner in the martian crust, they were likely not all formed in the same location on Mars. Additionally, the comparisons discussed in this paper between NWA 10169 and the enriched poikilitic shergottite NWA 7397 point towards this meteorite likely being a member from this enriched magmatic system. Meanwhile, the enriched shergottites Los Angeles, NWA 7320, and NWA 856, yield distinct ^{176}Lu/^{177}Hf source compositions than those of NWA 10169, RBT 04262, NWA 4468, LAR 06319, Shergotty, and Zagami (e.g., Udry et al., 2017). The crystallization and CRE ages of these two groups overlap, indicating that two spatially correlated magmatic systems, sampling two distinct enriched sources, were active contemporaneously within the interior of Mars, providing implications for the heterogeneity of the martian mantle (e.g., Nyquist et al., 2001; Eugster et al., 2010; Nishiizumi and Caffee, 2010; Wieler et al., 2016).

5. SUMMARY

- Northwest Africa 10169 has a coarse-grained, bimodal texture, and major and trace element mineral compositions that are reminiscent of the enriched poikilitic shergottites RBT 04262, GRV 020090, NWA 7397, and NWA 7755. The measured bulk REE profile shows one of the highest degrees of LREE-enrichment (La/Yb$_{CI}$ = 1.18) observed in the shergottite suite, and the initial εHf$_{(CHUR)}$ value of -17.5 suggests that NWA 10169 originated from an enriched source. Thus, NWA 10169 represents a new member of the geochemically enriched poikilitic shergottites.

- Based upon mineral textures, compositions and olivine P zonations and CSD profiles, I infer a crystallization history for NWA 10169 in which the chromite and olivine chadacrysts, began to crystallize from the parent magma and accumulate at depth in a magma staging chamber at relatively reducing conditions. The olivine chadacrysts were partially resorbed and subsequently enclosed by crystallizing pigeonite oikocrysts and began transit towards the surface. As the magma ascended towards the surface, the augitic oikocryst rims and the plagioclase, pyroxene, olivine, and ülvospinel of the non-poikilitic texture began to crystallize and continued until final emplacement, where the last pockets of melt crystallized late-stage phosphates, sulfides, and ilmenite under more oxidizing conditions. The preservation of P-zonation, and associated absence of Al zonation in olivine indicates a tentative cooling rate of ~ 10 °C/h during the growth of olivine, likely during transport towards the surface continuing until emplacement. This polybaric formation model is similar to the model proposed by Howarth et al. (2014) for the enriched poikilitic shergottite NWA 7397, and suggests a possible petrogenetic relationship with NWA 10169 and other poikilitic shergottites.

- This study introduces NWA 10169 as another member of the geochemically enriched shergottites with relatively reduced early-stage fO_2 values (FMQ -2.3) that overlap the fO_2 values of the geochemically intermediate shergottites. This finding, coupled with numerous recently reported shergottite fO_2 values (Fig. 13), indicates that the relationship between shergottite source enrichment and fO_2 is not as clear as was once thought. More work needs to be done to constrain the volatile contents and oxygen fugacities of the different geochemical sources of the shergottites.

- The estimated parental melt for NWA 10169 is similar to bulk Shergotty composition and the PTL compositions of olivine hosted melt inclusions in LAR 06319, possibly indicating similar parental magmas. Melt inclusions of NWA 10169 share Ca trends with RBT 04262, indicating fractionation of high-Ca pyroxene. Melt inclusions also preserve both K-poor and K-rich PTL compositions, a feature also observed in NWA 7397 and LAR 06319. The K/Ti ratios of these melt inclusions suggest that a K-rich melt from a metasomatized source was assimilated into the parent magma of NWA 10169, and likely NWA 7397 and LAR 06319 as well; providing implications for a similar magmatic history, and a possible petrogenetic link between these meteorites.

- The Lu-Hf crystallization age for NWA 10169 is 167 ± 31 Ma. This age is consistent with the Lu-Hf, Sm-Nd, and Rb-Sr ages determined for the other enriched shergottites and provides more evidence of relatively recent magmatic activity on Mars. The modeled source $^{176}Lu/^{177}Hf$ composition for NWA 10169 is identical, within error, to those of Shergotty, Zagami, LAR 06319, RBT 04262, and NWA 4468. As these meteorites have crystallization ages spanning 75 Ma, I suggest the presence of a persistent enriched

48

magmatic system sampled by each of these shergottites, with a reservoir distinct from the one sampled by the enriched shergottites Los Angeles, NWA 865, and NWA 7320.

Northwest Africa 10169 adds another member of the enriched poikilitic shergottites to our meteorite collection, and provides further evidence of young magmatic activity on Mars and a dynamic crystallization history across varying pressure and fO$_2$. The work presented in this study indicates not only a shared, long-lived geochemical source tapped by a subset of the enriched shergottites, but also a shared petrogenesis and magmatic history; thus revealing a tantalizing glimpse into a potential common magmatic system for NWA 10169 and this group of enriched shergottites.

APPENDIX A: TABLES

Table 1: Representative major element analyses of olivine and pyroxene in NWA 10169

	Olivine				Pigeonite			Augite	
	Poikilitic			Nonpoik.	Poikilitic		Nonpoik.	Poikilitic	Nonpoik.
oxide wt.%	Olivine in oik core	-------->	Olivine in oik rim		Oikocryst core	Oikocryst mantle			
SiO$_2$	37.6	36.9	36.2	36.2	54.4	52.8	52.2	52.1	51.9
TiO$_2$	-	<0.03	<0.03	-	0.07	0.19	0.35	0.26	0.34
Al$_2$O$_3$	<0.03	-	<0.03	-	0.44	0.86	1.00	1.60	1.90
Cr$_2$O$_3$	<0.05	<0.05	<0.05	<0.05	0.33	0.43	0.37	0.85	0.71
FeO$_T$	28.1	31.8	34.0	35.7	17.0	16.8	19.4	10.5	11.8
MnO	0.50	0.66	0.72	0.67	0.43	0.44	0.57	0.32	0.36
MgO	34.5	31.3	29.6	28.7	24.9	22.4	20.2	15.8	16.2
CaO	0.11	0.13	0.16	0.12	2.53	5.06	5.30	16.8	15.4
Na$_2$O	<0.03	-	-	<0.03	0.08	0.08	0.09	0.23	0.20
P$_2$O$_5$	<0.03	-	-	-	-	-	-	<0.03	-
NiO	0.09	<0.03	0.06	0.03	<0.03	0.06	-	<0.03	0.06
Total	100.9	100.9	100.8	101.4	100.2	99.0	99.5	98.5	98.8
Cations per 4 oxygen					*Cations per 6 oxygen*				
Si	1.00	1.00	0.99	0.99	1.98	1.96	1.96	1.96	1.95
Ti	-	<0.01	<0.01	-	<0.01	0.01	0.01	0.01	0.01
Al	<0.01	-	<0.01	-	0.02	0.04	0.04	0.07	0.08
Cr	<0.01	<0.01	<0.01	<0.01	0.01	0.01	0.01	0.03	0.02
Fe^{2+}	0.62	0.72	0.78	0.82	0.52	0.52	0.61	0.33	0.37
Mn	0.01	0.02	0.02	0.02	0.01	0.01	0.02	0.01	0.01
Mg	1.36	1.26	1.21	1.17	1.35	1.24	1.13	0.89	0.91
Ca	<0.01	<0.01	<0.01	<0.01	0.10	0.20	0.21	0.68	0.62
Na	<0.01	-	-	<0.01	0.01	0.01	0.01	0.02	0.01
P	-	-	-	-	-	-	-	-	-
Ni	<0.01	<0.01	<0.01	<0.01	<0.01	<0.01	-	<0.01	<0.01
Total	3.00	3.00	3.01	3.01	4.00	4.01	4.00	3.99	3.99
Fo	68.6	63.7	60.8	58.9					
Wo					5.0	10.3	10.9	35.7	32.6
En					68.6	63.2	57.9	46.8	47.8
Fs					26.3	26.6	31.2	17.5	19.6

FeO$_T$ = total iron, Fo = forsterite, Wo = wollastonite, En = enstatite, Fs = ferrosillite, - = zero

Table 2: Representative trace element analyses of olivine, pyroxene, maskelynite, and merrillite in NWA 10169

ppm	Olivine			Pigeonite		Augite		Maskelynite		Merrillite
	Poikilitic		Nonpoik.	Poikilitic	Nonpoik.	Poikilitic	Nonpoik.	Nonpoik.		
	Olivine in oik core	Olivine in oik rim		Oikocryst core		Oikocryt rim		Low-An	High-An	
Li	2.70	3.43	2.70	3.89	2.72	6.13	4.51	5.48	3.76	1.65
Sc	10.2	9.29	10.5	34.1	53.6	101	98.8	7.30	7.79	33.9
Ti	36.1	40.8	47.6	368	941	1154	1466	566	438	781
V	6.20	5.15	2.73	172	256	591	491	1.49	4.67	7.39
Cr	123	55.6	40.8	2279	2384	6431	4440	1.14	1.13	27.7
Co	79.6	68.6	73.3	46.2	47.0	39.5	28.6	0.289	0.334	1.89
Ni	383	318	261	165	127	155	99.6	0.415	0.801	4.15
Zn	56.7	55.1	77.4	54.1	69.9	39.4	33.6	3.55	4.14	3.34
Ga	0.135	0.149	0.205	1.64	3.98	4.91	6.65	97.1	55.8	1.79
Rb	-	0.013	0.026	0.005	0.013	0.163	0.202	22.7	5.25	0.918
Sr	0.006	0.025	0.307	0.249	0.589	9.29	12.3	227	193	115
Y	0.091	0.141	0.092	1.31	4.30	6.70	10.6	0.513	0.161	759
Zr	0.116	0.331	1.07	0.341	2.01	3.57	8.65	3.34	6.98	19.2
Nb	-	0.020	0.015	0.004	0.020	0.016	0.063	0.029	0.166	0.131
Cs	-	0.009	0.007	0.005	0.009	0.020	0.012	0.041	0.043	0.060
Ba	-	0.069	*3.13*	0.169	1.29	*95.5*	*76.7*	302.8	60.8	12.5
La	0.011	0.010	0.011	0.003	0.010	0.093	0.183	0.141	0.317	132.5
Ce	0.003	0.023	0.006	0.023	0.068	0.485	0.834	0.220	0.552	324.5
Pr	-	0.018	0.016	0.007	0.018	0.092	0.182	0.052	0.062	44.2
Nd	-	<0.003	0.008	0.044	0.134	0.696	1.13	0.049	0.300	202.4
Sm	0.010	0.006	0.003	0.027	0.152	0.400	0.748	-	0.043	73.0
Eu	0.003	0.029	0.036	0.007	0.052	0.178	0.262	0.929	0.663	20.7
Gd	0.019	0.005	0.046	0.098	0.353	0.708	1.35	0.015	0.048	110.3
Tb	<0.001	0.005	0.002	0.019	0.080	0.176	0.282	0.019	0.008	20.4
Dy	0.006	0.052	0.008	0.197	0.649	1.24	2.07	0.006	0.151	135.8
Ho	0.003	0.023	0.017	0.058	0.172	0.291	0.451	0.002	0.006	28.9
Er	0.020	0.041	0.021	0.131	0.510	0.764	1.21	-	<0.004	74.4
Tm	0.009	0.026	0.008	0.026	0.079	0.115	0.170	-	0.003	10.1
Yb	0.050	0.098	0.078	0.195	0.619	0.757	1.04	0.009	0.030	63.5
Lu	0.011	0.026	0.016	0.021	0.093	0.111	0.149	0.003	0.004	8.31
Hf	0.002	0.022	0.041	0.021	0.093	0.185	0.459	0.105	0.167	0.331
Ta	0.004	0.012	0.002	0.001	<0.001	-	0.001	0.093	0.030	0.024
Th	0.008	0.010	0.005	-	<0.001	0.001	0.006	0.015	0.027	18.8
U	<0.001	0.020	0.02	<0.001	0.001	0.006	0.007	0.033	0.020	3.29

oik = oikocryst, An = anorthite, - = zero

values in italics are likely altered through terrestrial contamination

Table 3: Representative microprobe analyses of maskelynite, Fe-Cr-Ti oxides, and phosohates in NWA 10169

oxide wt.%	Maskelynite				Fe-Cr-Ti oxide				Merrillite	
	Low-An	High-An	High-Or		Chr-rich	Spn-rich	Ulv-rich			
SiO_2	57.9	54.6	58.8	SiO_2	0.14	0.06	<0.03	SiO_2	0.19	0.18
TiO_2	0.05	0.05	0.05	TiO_2	0.72	2.61	17.9	Ce_2O_3	0.05	0.04
Al_2O_3	26.1	28.6	25.1	Al_2O_3	5.99	10.9	3.52	FeO_T	1.46	1.12
FeO_T	0.41	0.59	0.41	Cr_2O_3	58.4	46.3	18.5	MgO	2.99	3.29
MnO	-	<0.05	-	Fe_2O_3	2.65	5.88	13.2	CaO	46.7	46.7
MgO	0.07	0.08	0.08	FeO	29.0	30.9	44.0	Na_2O	2.14	1.95
CaO	7.66	10.9	6.94	MnO	0.71	0.61	0.69	K_2O	0.08	0.06
Na_2O	6.49	4.99	5.93	MgO	3.12	3.30	2.64	P_2O_5	46.4	46.5
K_2O	0.88	0.37	2.14	NiO	<0.03	0.03	<0.03	Cl	<0.03	-
P_2O_5	0.11	<0.03	0.13	Na_2O	<0.03	-	-	Total	100.1	99.8
Total	99.7	100.1	99.6	Total	100.7	100.6	100.4			
Cations per 8 oxygen				*Cations per 4 oxygen*				*Cations per 28 oxygen*		
Si	2.61	2.46	2.65	Si	<0.01	<0.01	<0.01	Si	0.03	0.03
Ti	<0.01	<0.01	<0.01	Ti	0.02	0.07	0.48	Ce	<0.01	<0.01
Al	1.38	1.52	1.33	Al	0.25	0.44	0.15	Fe	0.22	0.17
Fe^{2+}	0.02	0.02	0.02	Cr	1.62	1.26	0.53	Mg	0.80	0.88
Mn	-	<0.01	-	Fe^{3+}	0.07	0.15	0.36	Ca	8.96	8.95
Mg	<0.01	0.01	0.01	Fe^{2+}	0.85	0.89	1.32	Na	0.74	0.67
Ca	0.37	0.53	0.34	Mn	0.02	0.02	0.02	K	0.02	0.01
Na	0.57	0.44	0.52	Mg	0.16	0.17	0.14	P	7.03	7.04
K	0.05	0.02	0.12	Ni	<0.01	<0.01	<0.01	Cl	<0.01	-
P	<0.01	<0.01	0.01	Na	<0.01	-	-	Total	17.80	17.75
Total	5.00	5.00	4.99	Total	3.00	3.00	3.00			
Or	5.1	2.2	12.6	Chr	85.0	68.6	32.0			
An	37.5	53.5	34.4	Ulv	2.0	7.4	58.9			
Ab	57.4	44.4	53.0	Spn	13.0	24.0	9.1			

FeO_T = total iron, Or = orthoclase, An = anorthite, Ab = albite, Chr = chromite, Ulv = ulvöspinel, Spn = spinel, - = zero

Table 4: Crystal size distribution results for thin section 1 of NWA 10169

Population	No. of grains	Shape	R^2	Orientation	Avg. size (mm)	Slope (mm^{-1})	Intercept	Residence Time (Earth days)[a]
Total	506	1.00:1.25:1.90	0.90	length	0.31	-3.55	3.91	105
				width	0.19	-4.79	4.69	78
Poikilitic	141	1.00:1.40:2.20	0.88	length	0.25	-4.53	3.14	82
Non-poikilitic	361	1.00:1.30:2.10	0.89	length	0.34	-3.41	3.50	109

[a] Used the estimated growth rate of 3.1×10^{-8} mm/s (Basu Sarbadhikari et al., 2009)

Table 5: Lu-Hf isotopic data for NWA 10169

Sample	$^{176}Lu/^{176}Hf$	% unc	$^{176}Hf/^{176}Hf$	% unc	$^{176}Hf/^{176}Hf_i$	±2 SD	εHf_i[a]	Isochron age	±2 SD	$^{176}Lu/^{176}Hf_{source}$[b]	±2 SD
S1-WR	0.01754	0.2	0.282246	0.005	0.282186	0.000011	-17.5	167	31	0.02748	0.00037
S2-WR*	0.01286	0.2	0.282214	0.005							
S3-pyx	0.03368	0.2	0.282293	0.005							
S4-mask	0.01059	0.2	0.282225	0.005							
S5-oxide	0.00071	0.2	0.282191	0.005							

[a] the initial εHf value was calculated using the CHUR parameters of Bouvier et al. (2008b).

[b] 176Lu/176Hf$_{source}$ was calculated using the source differentiation age of Borg et al. (2016), and the CHUR parameters of Bouvier et al. (2008b)

WR = whole rock, WR* = whole rock minus separates, pyx = pyroxene, mask = maskelynite

Table 6: NWA 10169 parent melt and bulk compositions estimated from melt inclusions and pyroxene compositions

	Melt inclusion PBC[b]								
oxide wt.%	MI1[a]	MI5	MI10	MI15	MI19	MI6			
SiO_2	61.8	54.1	63.6	50.9	61.8	61.8			
TiO_2	1.00	1.20	0.90	1.91	0.85	1.28			
Al_2O_3	13.2	8.73	13.4	12.9	13.4	14.1			
Cr_2O_3	0.08	0.05	0.06	1.37	<0.05	<0.05			
FeO_T	5.97	11.1	6.83	8.83	7.69	7.06			
MnO	0.21	0.43	0.23	0.33	0.25	0.10			
MgO	6.15	11.8	5.68	3.87	6.39	2.37			
CaO	10.1	8.46	7.79	5.99	7.87	9.14			
Na_2O	0.18	0.11	0.20	3.69	0.17	0.16			
K_2O	0.21	1.59	0.24	5.01	0.16	1.30			
P_2O_5	0.87	1.86	0.52	4.12	0.79	1.16			
SO_3	-	0.12	0.14	0.13	0.25	0.27			
Cl	-	-	<0.03	0.21	-	0.06			
Total	99.7	99.5	99.6	99.3	99.7	98.8			
Mg#	64.7	65.5	59.7	43.9	59.7	37.4			

	Melt inclusion PTL[c] Fe-Mg corrected						NWA 10169	Shergotty	LAR 06319
oxide wt.%	MI1[a]	MI5	MI10	MI15	MI19	MI6	WR	WR[d]	MI[e]
host olivine	Fo66	Fo63	Fo61	Fo61	Fo61	Fo59	n/a	n/a	Fo66
FeO_T melt	19.40	18.52	18.41	18.41	18.41	18.37	n/a	n/a	19.25
SiO_2	53.7	52.7	56.8	47.5	56.1	55.1	48.0	51.3	52.29
TiO_2	0.72	1.18	0.71	1.55	0.69	0.97	0.54	0.82	0.99
Al_2O_3	9.54	8.61	10.5	10.5	10.9	10.6	4.57	6.88	9.96
Cr_2O_3	0.06	0.05	0.05	1.11	<0.05	<0.05	n/a	0.20	0.16
Fe_2O_3	0.81	1.75	1.33	2.57	1.32	1.53	n/a	n/a	2.14
FeO or FeO_T	18.7	16.9	17.2	16.3	17.2	17.1	21.6	19.40	17.32
MnO	0.15	0.42	0.18	0.27	0.20	0.08	0.50	0.52	0.19
MgO	8.15	6.49	6.32	4.98	6.27	5.78	19.34	9.30	7.09
CaO	7.28	8.34	6.12	4.86	6.39	6.89	3.97	9.60	5.24
Na_2O	0.13	0.11	0.16	3.00	0.14	0.12	0.96	1.39	1.04
K_2O	0.15	1.57	0.19	4.07	0.13	0.98	0.11	0.17	2.91
P_2O_5	0.63	1.83	0.41	3.35	0.64	0.88	0.40	0.67	0.67
Total	100.0	100.0	100.0	100.0	100.0	100.0	100.0	100.3	100.0
Mg#	43.8	40.6	39.6	35.3	39.3	37.6	61.5	46.1	42.2

[a] MI1 is entrapped within a poikilitic olivine chadacryst, and represents the estimated parent melt of NWA 10169.

[b] The present bulk compositions (PBC) of melt inclusions were calculated through X-ray maps (Fig. 4).

[c] The primary trapped liquid (PTL) compositions of melt inclusions were calculated by correcting for Fe-Mg exchange with the host olivine in PETROLOG3, assuming original melt FeO_T content (Danyushevsky et al., 2001, 2011).

[d] Bulk major element composition for Shergotty from Lodders (1998)

[e] The PTL compositions of melt inclusions hosted by Fo66 olivine of LAR 06319 (Peslier et al., 2010)

FeO_T = total iron, Fo = forsterite, MI = melt inclusion, n/a = not analyzed, - = zero
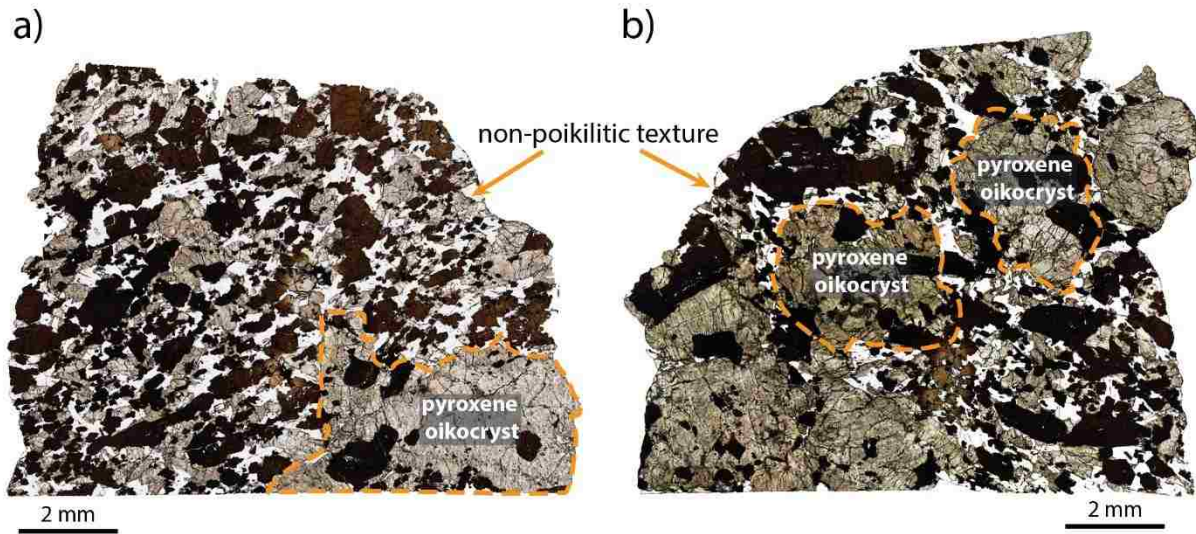
Figure 1. Plane polarized light photomicrographs of (a) slide 1 and (b) slide 2 of NWA 10169. Yellow dashed lines outline pyroxene oikocrysts.
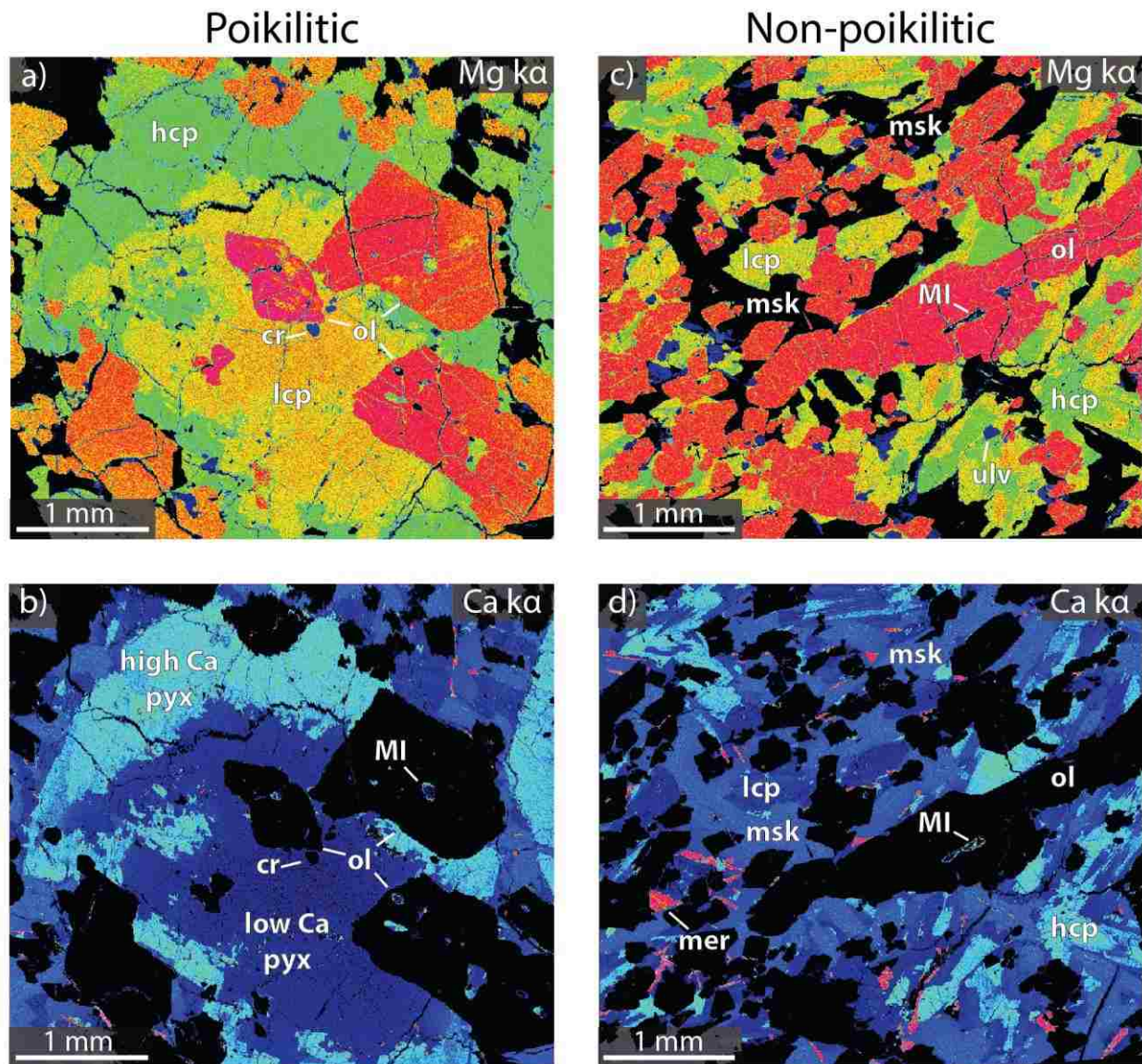
Figure 2. Ca kα and Mg kα X-ray maps of both the poikilitic and non-poikilitic textures. (a and b) Mg and Ca X-ray maps of a typical zoned (low-Ca to high-Ca) pyroxene oikocryst with olivine chadacrysts decreasing in forsterite content towards the oikocryst rims. (c) Mg and (d) Ca X-ray maps of a typical region of non-poikilitic texture. Lcp = low-Ca pyroxene; hcp = high-Ca pyroxene; ol = olivine; cr = chromite; ulv = ulvöspinel; msk = maskelynite; mer = merrillite; MI = melt inclusion.
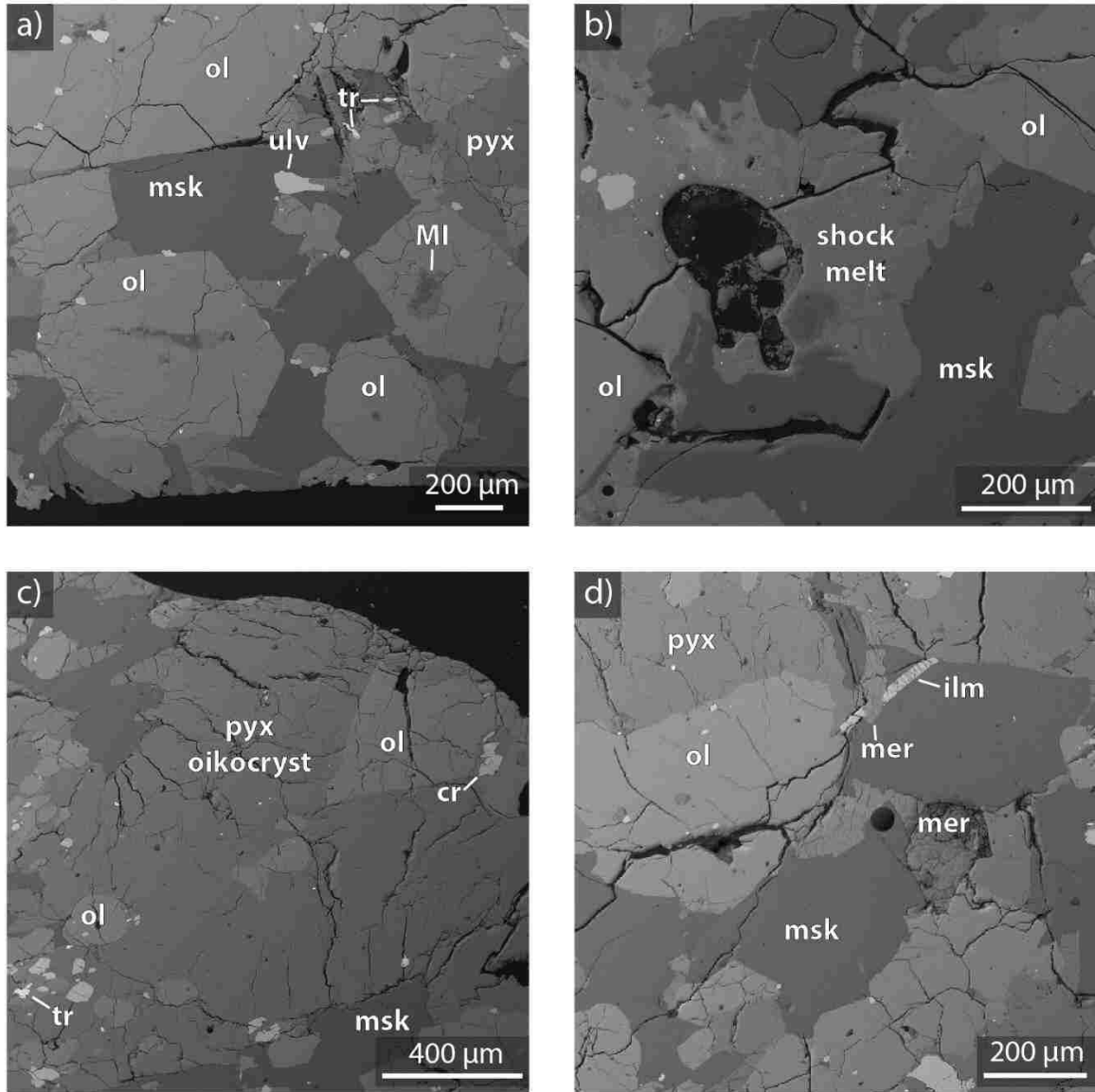
Figure 3. Backscatter electron images (BSE) of different regions of interest within NWA 10169. (a) An area of non-poikilitic texture showing euhedral olivine shapes and olivine-hosted melt inclusions. (b) A shock melt pocket in the non-poikilitic texture. (c) One of the smaller pyroxene oikocrysts with olivine chadacrysts ranging from subhedral to anhedral, showing characteristics of adsorption. (d) A group of late stage minerals in the non-poikilitic texture, with a large, highly fractured merrillite grain and an elongate ilmenite grain. Pyx = pyroxene; ol = olivine; cr =

chromite; tr = troilite; ulv = ulvöspinel; msk = maskelynite; ilm = ilmenite; mer = merrillite; MI = melt inclusion.
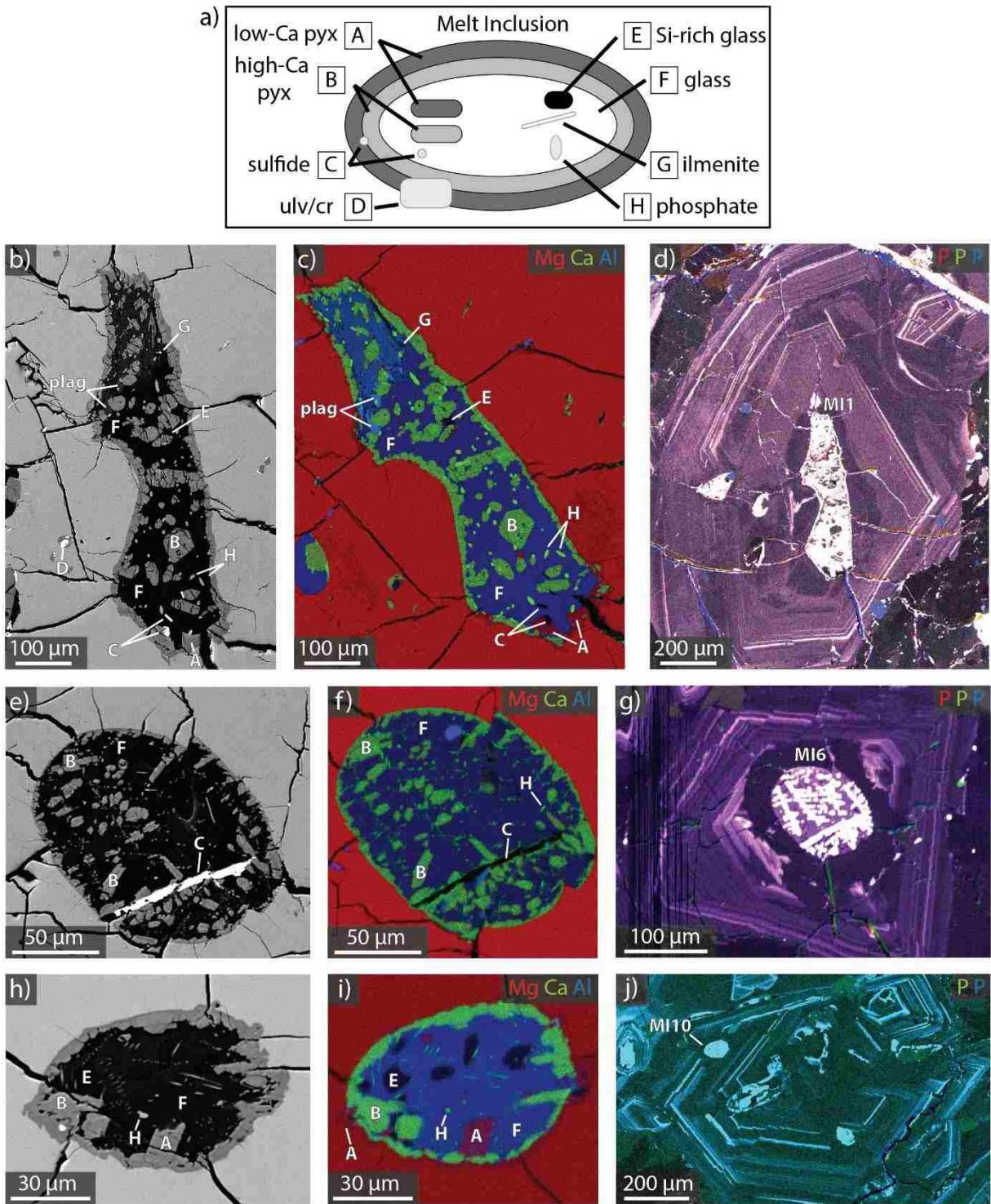
Figure 4. Images of melt inclusions and their respective host olivine. (a) A schematic of a typical melt inclusion in NWA 10169, with labels for commonly observed phases; pyx = pyroxene; cr =

chromite; ulv = ulvöspinel; modified from Peslier et al. (2010). (b) BSE image and (c) a Mg, Ca, Al composite X-ray map of MI1 within a poikilitic Fo_{66} olivine chadacryst, the most primitive olivine in NWA 10169 with a measurable melt inclusion. (d) A composite P X-ray map (from P measured on the PET, TAP, and LPET crystals) of MI1's host olivine, showing the melt inclusion in the core of the host olivine, continuous zonation in the interior of the olivine, and discontinuous zonation near the rim. (e) BSE image and (f) a Mg, Ca, Al composite X-ray map of MI6 within a non-poikilitic Fo_{59} olivine. (g) A composite P X-ray map of MI6's host olivine, showing MI6 in the low-P core of its host olivine, and dislocations of the P zonation from shock. (h) BSE image and (i) a Mg, Ca, Al composite X-ray map of MI10 within a non-poikilitic Fo_{61} olivine. (j) A composite P X-ray map (from PET and TAP crystals) of MI10's host olivine, showing MI10 trapped near the rim of the olivine, and multiple nucleation sites of olivine with low to high-P cores. Plag = plagioclase; MI = melt inclusion.
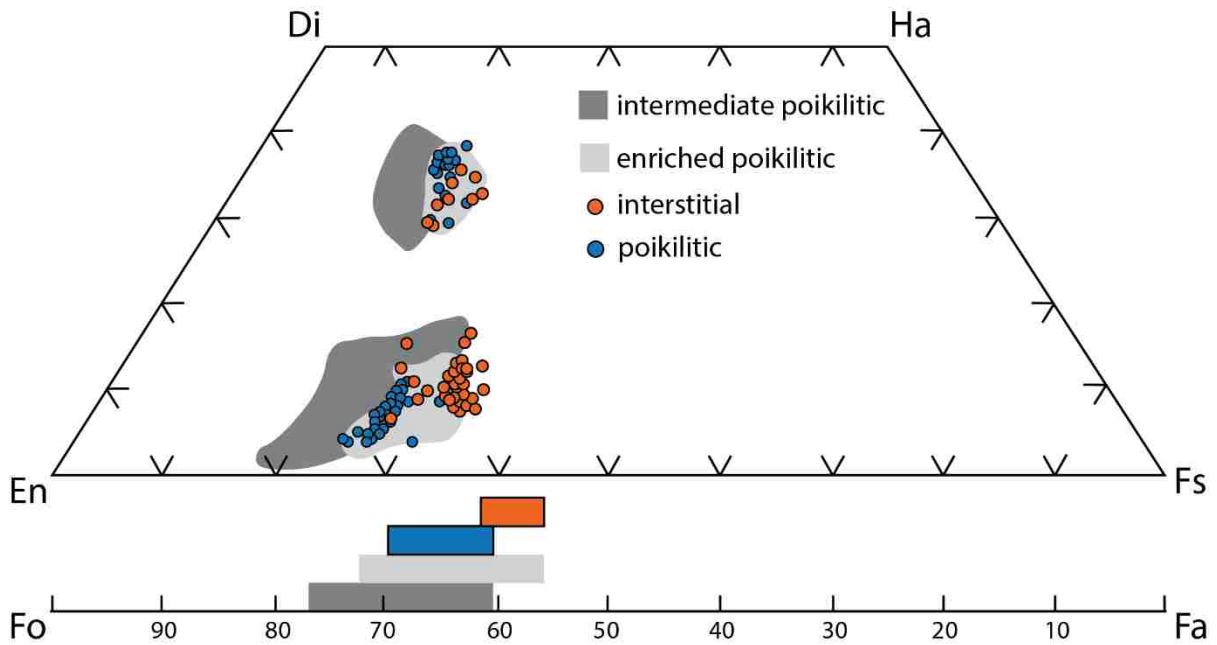
Figure 5. Pyroxene quadrilateral and olivine major element compositions for NWA 10169. Compositional fields for the intermediate poikilitic shergottites are from Mikouchi et al. (2005, 2008). Compositional fields for the enriched poikilitic shergottites are from Bingkui et al. (2004), Usui et al. (2010), and Howarth et al. (2014).
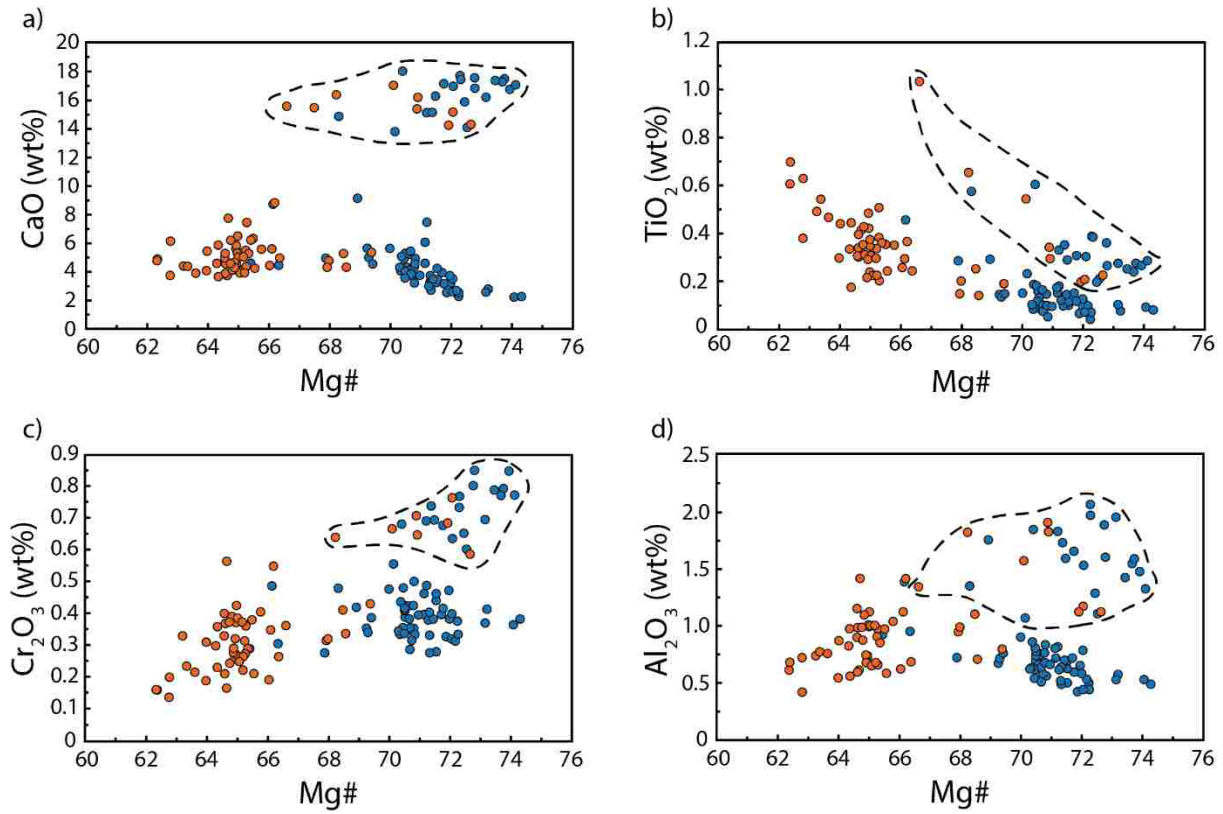
Figure 6. Variation of (a) CaO, (b) TiO₂, (c) Cr₂O₃, and (d) Al₂O₃ with Mg# in NWA 10169 pyroxene. Blue dots represent pyroxene oikocrysts, and orange dots represent interstitial, non-poikilitic pyroxene. The black dashed outline surrounds high-Ca pyroxene analyses.
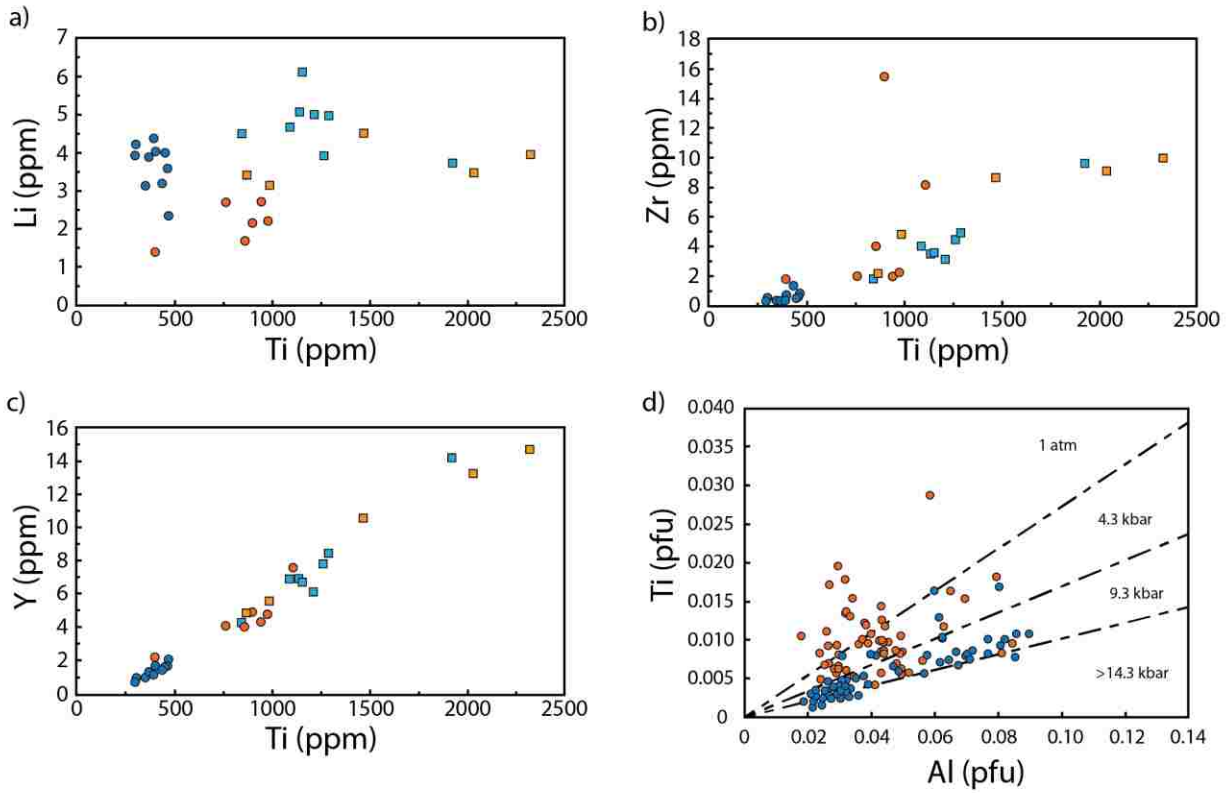
Figure 7. Variation of the trace elements (a) Li, (b) Zr, and (c) Y with Ti in NWA 10169 pyroxene. Blue points represent pyroxene oikocrysts, and orange points represent interstitial, non-poikilitic pyroxene. The circles represent low-Ca pyroxene analyses, while the squares represent high-Ca pyroxene analyses. (d) Ti versus Al contents in NWA 10169 pyroxene, plotted on experimentally calibrated isobars from Nekvasil et al. (2004) and Filiberto et al. (2010).
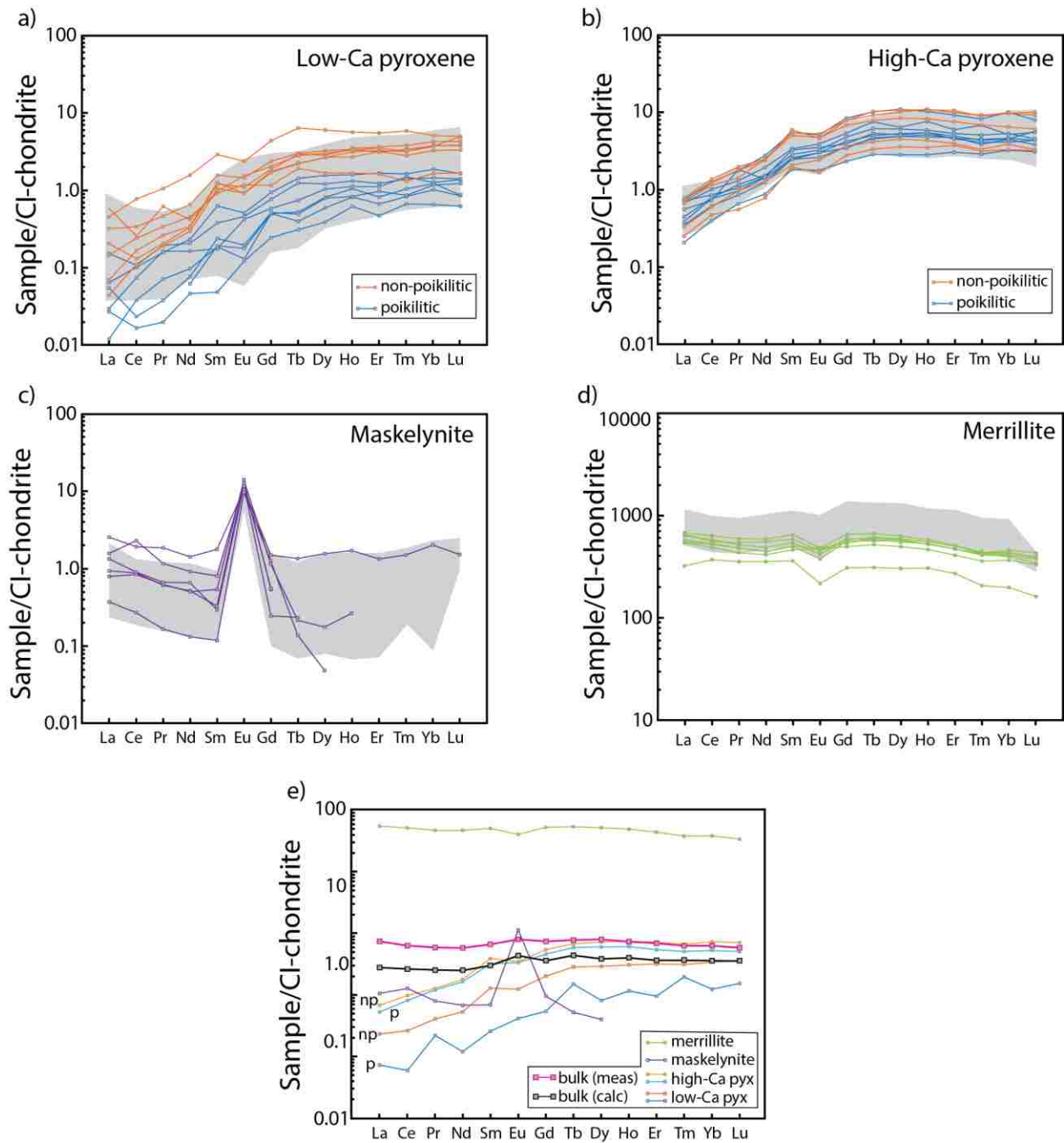
Figure 8. Rare earth element (REE) compositions of NWA 10169 (a) low-Ca and (b) high-Ca pyroxene, normalized to CI chondrites (McDonough and Sun, 1995). Chondrite-normalized REE profiles for (c) maskelynite and (d) merrillite. (e) Average chondrite-normalized REE profiles for pyroxene, maskelynite, and merrillite, as well as the calculated (black) and measured (pink) bulk REE profiles for NWA 10169. Grey envelopes correspond to the REE profiles of minerals from

enriched poikilitic shergottites NWA 7755, NWA 7397, RBT 04262, and GRV 020090 (Usui et al., 2010; Jiang and Hsu, 2012; Howarth et al., 2014; Howarth at al., 2015). P = poikilitic, np = non-poikilitic.
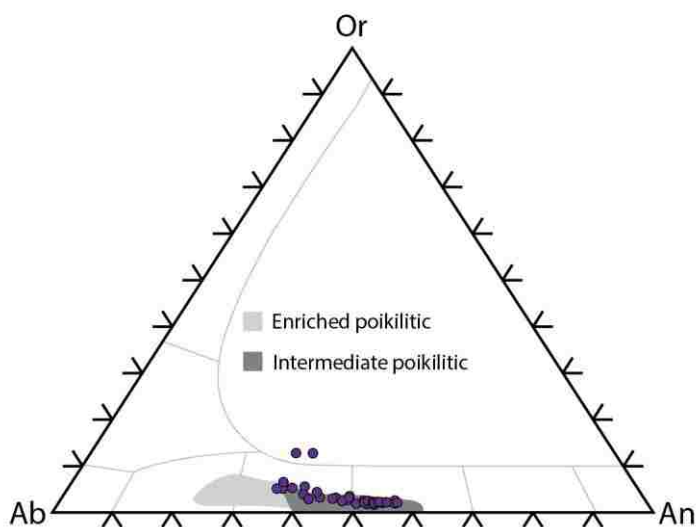
Figure 9. Maskelynite major element compositions in NWA 10169 plotted on the An-Ab-Or ternary. The intermediate poikilitic shergottite fields are from Allan Hills (ALH)A 77005, LEW 88516, Y-793605, and NWA 1950 (Harvey et al., 1993; Mikouchi and Miyamoto, 1997; Mikouchi, 2005). The enriched poikilitic shergottite fields are from RBT 04261/2, GRV 020090, and NWA 7755 (Usui et al., 2010; Jiang and Hsu, 2012; Howarth et al., 2015).
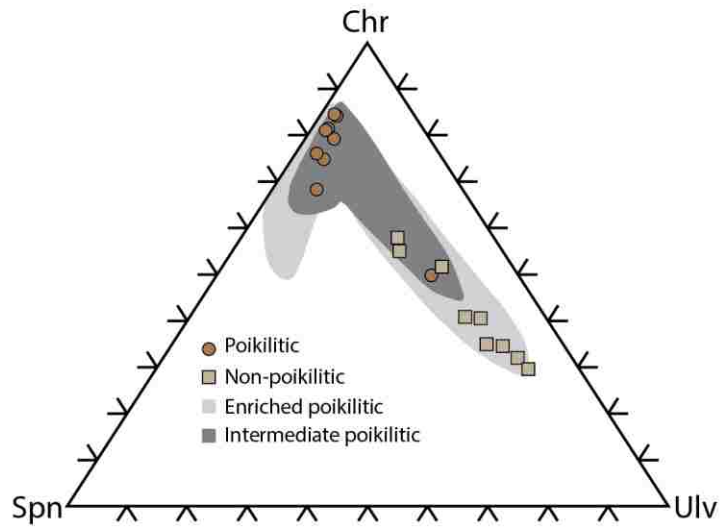
Figure 10. Spinel compositional data from NWA 10169 plotted on the Ulv-Chr-Spn ternary. The intermediate poikilitic shergottite fields are from NWA 4797 (Walton et al., 2012). The enriched poikilitic shergottite fields are from RBT 04261/2, GRV 020090, and NWA 7755 (Usui et al., 2010; Jiang and Hsu et al., 2012; Howarth et al., 2015).
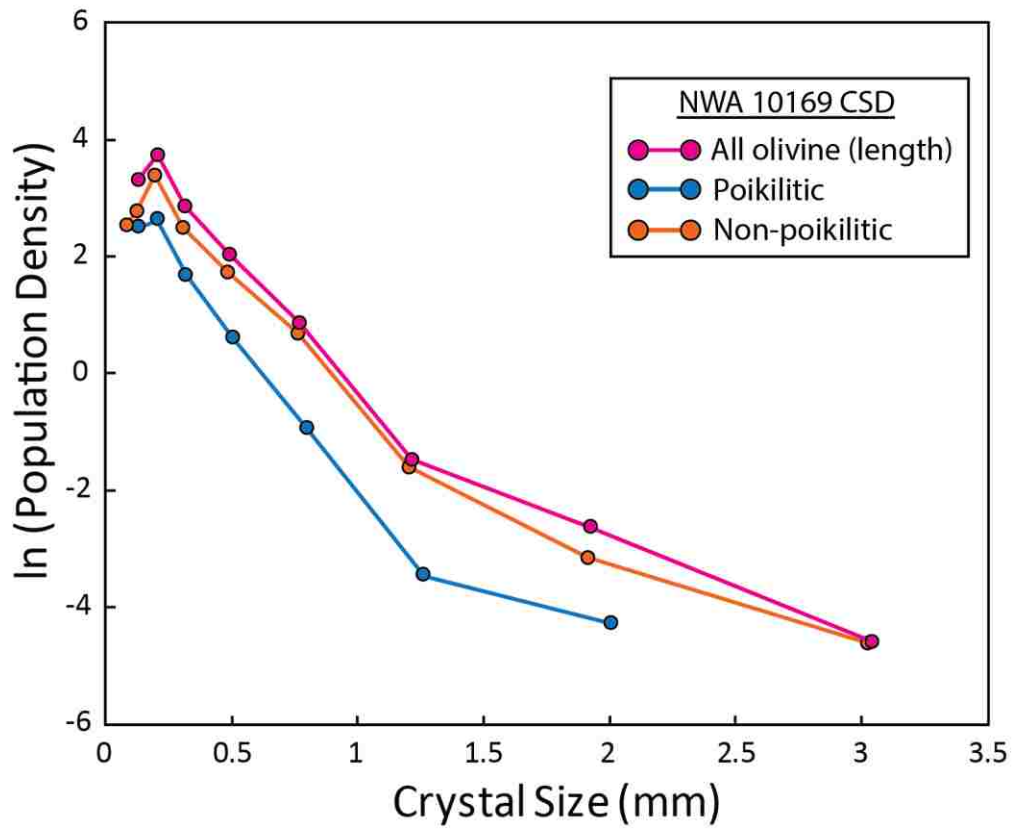
Figure 11. Crystal Size Distribution plot with olivine population density plotted against the crystal size for all NWA 10169 olivine (pink), non-poikilitic olivine (orange), and olivine chadacrysts (blue). All CSD profiles plotted are based on the length axis of olivine crystals.
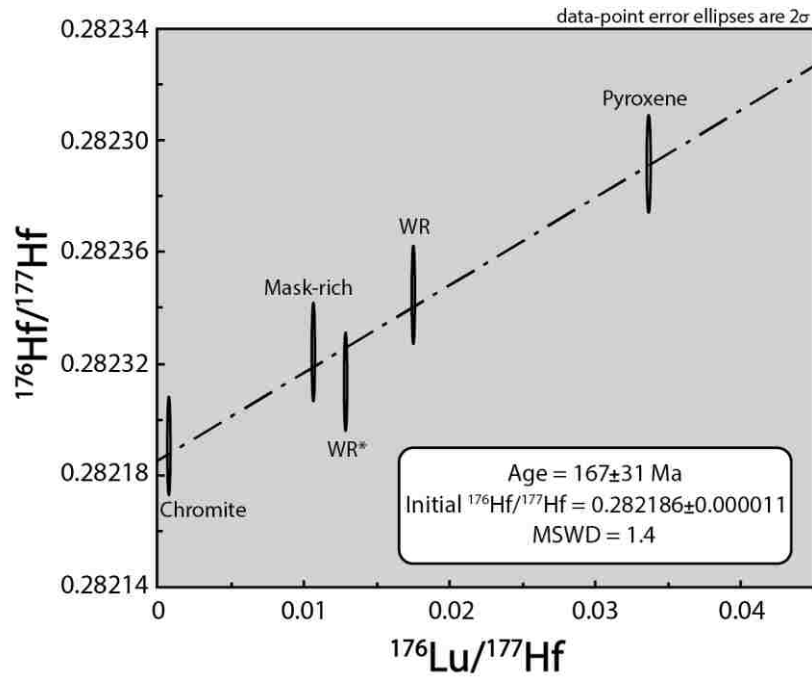
Figure 12. Five-point Lu-Hf isochron calculated with *Isoplot.* MSWD = mean standard weighted

deviation, mask = maskelynite, WR = whole rock, WR* = whole rock minus mineral separates.
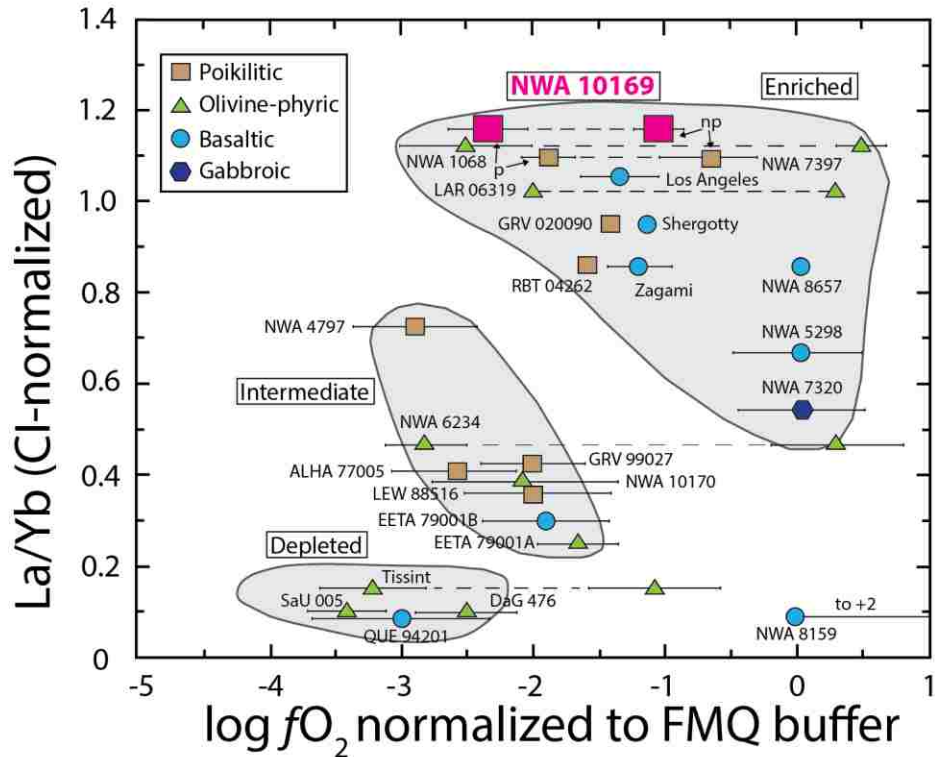
Figure 13. Oxygen fugacities relative to the FMQ buffer, for NWA 10169 and other shergottites, versus chondrite-normalized La/Yb ratio as a proxy for LREE enrichment. Data for the basaltic shergottites are from Lodders (1998), Rubin et al. (2000), Herd et al. (2001), Hui et al. (2011), and Howarth et al. (2018). Data for the olivine-phyric shergottites are from Dreibus et al. (2000), Zipfel et al. (2000), Barratt et al. (2002), Herd et al. (2003), Herd (2006), Peslier et al. (2010), Gross et al. (2013), Castle and Herd (2017), and Howarth and Udry (2017). Data for the poikilitic shergottites are from Goodrich et al. (2003), Lin et al. (2005), Usui et al. (2010), Jiang and Hsu (2012), Walton et al. (2012), and Howarth et al. (2014). Data for NWA 7320 and NWA 8159 are from Udry et al. (2017) and Herd et al. (2017), respectively.

71

Figure 14. Chondrite-normalized REE profiles for NWA 10169, intermediate poikilitic shergottites (black), and other enriched shergottites (gray). Data for the enriched poikilitic shergottites are from Usui et al. (20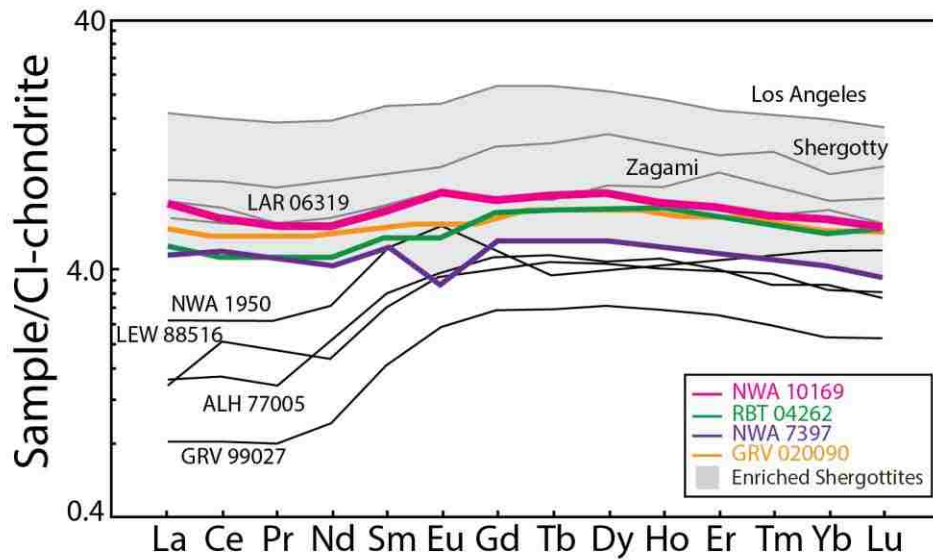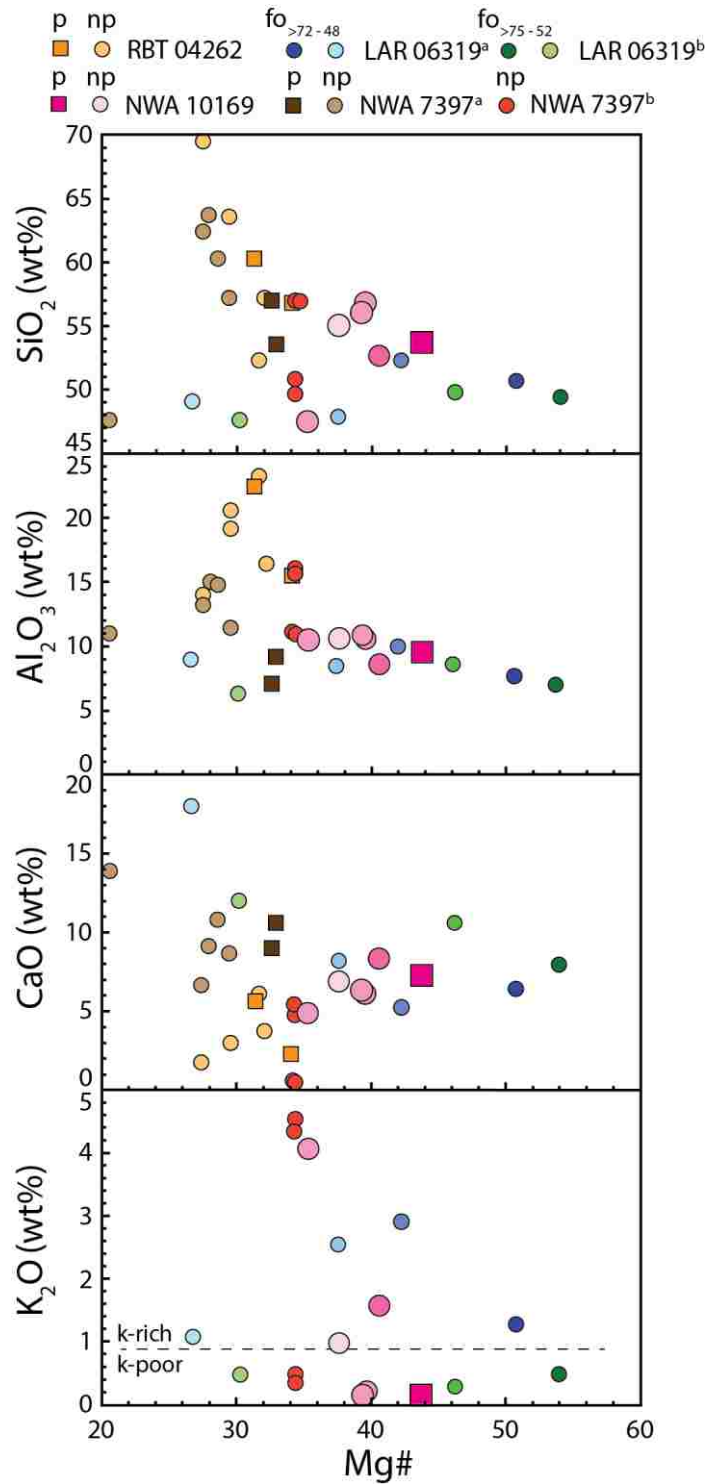10), Jiang and Hsu et al. (2012), and Howarth et al. (2014). Data for the intermediate poikilitic shergottites are from Lodders (1998), Gillet at al. (2005), and Lin et al. (2005). Data for Zagami and Shergotty are from Lodders (1998), LAR 06319 is from Basu Sarbadhikari et al. (2009), and Los Angeles is from Jambon et al. (2002).

Figure 15. The Mg# of calculated primary trapped liquid compositions of NWA 10169 melt inclusions, plotted against SiO_2, Al_2O_3, and CaO wt. %. Lighter colors correspond to lower host olivine fo-content. Data for the enriched poikilitic shergottites RBT 04262, NWA 7397[a], and NWA

7397[b] are from Potter et al. (2015), Ferdous et al. (2018), and He and Xiao (2014), respectively. Data for LAR 0619[a] and LAR 06319[b] are from Peslier et al. (2010) and Basu Sarbadhikari et al. (2011), respectively. P = poikilitic, np = non-poikilitic.
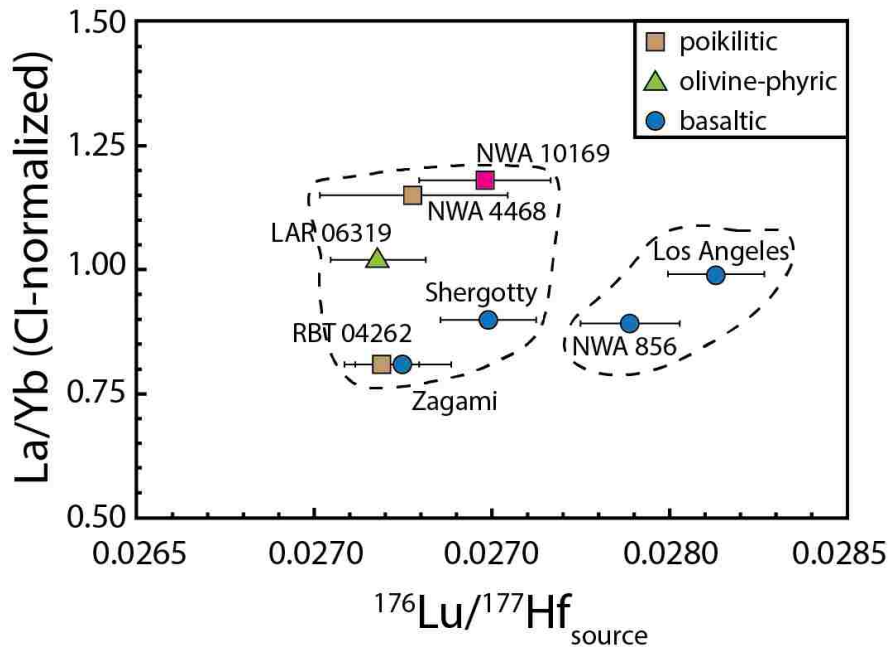
Figure 16. Modeled $^{176}\text{Lu}/^{177}\text{Hf}_{\text{source}}$ plotted against LREE enrichment, showing two disctinct sources for the enriched shergottites. Bulk REE data from Lodders (1998), Rubin et al. (2000), Jambon et al. (2002), Anand (2008), and Basu Sarbadhikari et al. (2009). Lu-Hf isotope used for modeling from Nekvasil et al. (2001), Brandon et al. (2004), Bouvier et al. (2005, 2008a), Debaille et al. (2008), Lapen et al. (2008, 2009), and Shafer et al. (2010). NWA 7320 likely shares a source with Los Angeles and NWA 856 (Udry et al., 2017).
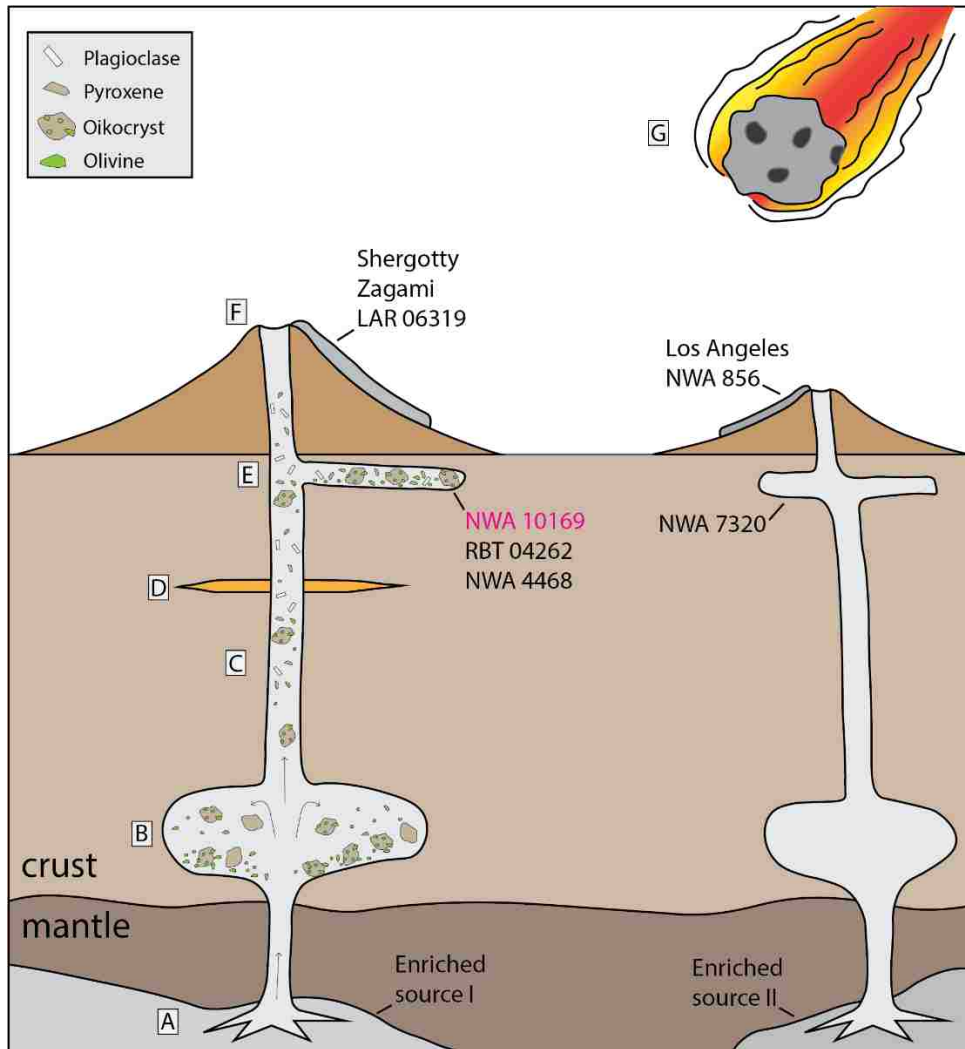
Figure 17. Schematic of a petrogenetic model for NWA 10169 and the enriched shergottites. A) Partial melting of two distinct enriched sources generating two different magma systems. B) Ponding of magma near the base of the martian crust at ~ 10 kbar, followed by crystallization, accumulation of pyroxene oikocrysts and olivine, and entrapment of MI1. C) Transport towards the surface, initiation of non-poikilitic crystallization, progressive auto-oxidation, and possible degassing. D) Assimilation of K-rich, metasomatized crustal rocks, and entrapment of MI15. E) Emplacement in the crust and final crystallization of the late-stage non-poikilitic material of the enriched poikilitic shergottites. F) Eruption of the extrusive enriched shergottites onto the surface

76

of Mars. G) Ejection of the two groups of enriched shergottites from the martian atmosphere based on overlapping CRE ages (e.g., Eugster et al., 2010).

REFERENCES

Anand M., James S., Greenwood R. C., Johnson D., Franchi I. A., and Grady M. M. (2008) Mineralogy and geochemistry of shergottite RBT 04262. *Lunar and Planetary Science Conference XXXIX,* abstract #2173.

Asimow P. D., and Ghiorso M. S. (1998) Algorithmic modifications extending MELTS to calculate subsolidus phase relations. *American Mineralogist,* **83**, 1127-1132.

Ballhaus C., Berry R. F., and Green, D. H. (1991) High pressure experimental calibration of the olivine-orthopyroxene-spinel oxygen geobarometer: implications for the oxidation state of the upper mantle. *Contributions to Mineralogy and Petrology*, **107**, 27–40.

Balta J. B., Sanborn M., and McSween H. Y. (2013) Magmatic history and parental melt composition of olivine-phyric shergottite LAR 06319: Importance of magmatic degassing and olivine antecrysts in Martian magmatism. *Meteoritics & Planetary Science*, **48**, 1359-1382.

Balta J. B., Sanborn M. E., Udry A., Wadhwa M., and McSween H. Y. (2015) Petrology and trace element geochemistry of Tissint, the newest shergottite fall. *Meteoritics & Planetary Science,* **50**, 63-85.

Balta J. B., Sanborn M. E., Mayne R. G., Wadhwa M., McSween H. Y., and Crossley S. D. (2016) Northwest Africa 5790: A previously unsampled portion of the upper part of the nakhlite pile. *Meteoritics & Planetary Science,* **52**, 36-59.

Bard J. P., (1986) Microtextures of igneous and metamorphic rocks. *Petrology and Structural Geology,* D. Reidel Publishing Company, Dordrecht, 248.

Barrat J. A., Jambon A., Bohn M., Gillet P_H., Sautter V., Göpel C., Lesourd M., and Keller F. (2002) Petrology and chemistry of the Picritic Shergottite North West Africa 1068 (NWA 1068). *Geochimica et Cosmochimica Acta*, **66**, 3505-3518.

Basu Sarbadhikari A., Day J. M. D., Liu Y., Rumble D. III., and Taylor L. A. (2009) Petrogenesis of olivine-phyric shergottite Larkman Nunatuk 06319: Implications for enriched components in Martian basalts. *Geochimica et Cosmochimica Acta*, **73**, 2190-2214.

Basu Sarbadhikari A., Goodrich C. A., Liu Y., Day J. M. D., and Taylor, L. A. (2011) Evidence for heterogeneous enriched shergottite mantle sources in Mars from olivine-hosted melt inclusions in Larkman Nunatak 06319. *Geochimica et Cosmochimica Acta*, **75**, 6803–6820.

Baziotis I., Asimow P. D., Ntaflos T., Boyce J. W., McCubbin F. M., Koroneos A., Perugini D., Flude S., Storey M., Liu Y. S., Klemme S., and Berndt J. (2017) Phosphorus zoning as a recorder of crystal growth kinetics: application to second-generation olivine in mantle xenoliths from the Cima Volcanic Field. *Contributions to Mineralogy and Petrology,* **172**, s00410-017-1376-7.

Bingkui M., Ziyuan O., Daode W., Yitai J., Guiqin W., and Yangting, L. (2004) A New Martian Meteorite from Antarctica: Grove Mountains (GRV) 020090. *Acta Geologica Sinica,* **78**, 1034-1041.

Bloch E., and Ganguly J. (2014) ^{176}Lu-^{176}Hf and ^{147}Sm-^{143}Nd ages of the Martian shergottites: Evaluation of the shock-resetting hypothesis through diffusion kinetic experiments and modeling, and petrological observations. *Earth and Planetary Science Letters,* **395**, 173-183.

Bouvier A., Blichert-Toft J., Vervoort J. D., and Albaréde F. (2005) The age of SNC meteorites and the antiquity of the Martian surface. *Earth and Planetary Science Letters,* **240**, 221-233.

Bouvier A., Blichert-Toft J., Vervoort J. D., Gillet P., and Albaréde F. (2008a) The case for old basaltic shergottites. *Earth and Planetary Science Letters,* **266**, 105-124.

Bouvier A., Vervoort J. D., and Patchett P.J. (2008b) The Lu-Hf and Sm-Nd isotopic composition of CHUR: Constraints from unequilibrated chondrites and implications for the bulk compositions of terrestrial planets. *Earth and Planetary Science Letters,* **273**, 48-57.

Bouvier A., Blichert-Toft J., and Albaréde F. (2009) Martian meteorite chronology and the evolution of the interior of Mars. *Earth and Planetary Science Letters,* **280**, 285-295.

Borg L. E., Nyquist L. E., Taylor L. A., Wiesmann H., and Shih C. -Y. (1997) Constraints on Martian differentiation processes from Rb-Sr and Sm-Nd isotopic analyses of the basaltic shergottite QUE 94201. *Geochimica et Cosmochimica Acta*, **61**, 4915-4931.

Borg L. E., Norman M., Nyquist L. E., Bogard D., Snyder G., Taylor L. A., and Lindstrom M. (1999) Isotopic studies of ferroan anorthosite 62236: a young lunar crustal rock from a light rare-earth-element-depleted source. *Geochimica et Cosmochimica Acta,* **63**, 2679-2691.

Borg L. E., Nyquist L. E., Wiesmann H., Shih C. -Y., and Reese Y. (2003) The age of Dar al Gani 476 and the differentiation history of the martian meteorites inferred from their radiogenic isotopic systematics. *Geochimica et Cosmochimica Acta,* **67**, 3519-3536.

Borg L. E., Edmunson J. E., and Asmerom Y. (2005) Constraints on the U-Pb isotopic systematics of Mars inferred from a combined U-Pb, Rb-Sr, and Sm-Nd isotopic study of the Martian meteorite Zagami. *Geochimica et Cosmochimica Acta,* **69**, 5819-5830.

Borg L. E., Gaffney A. M., and Depaolo D. J. (2008) Preliminary Age of Martian Meteorite Northwest Africa 4468 and Its Relationship to the Other Incompatible-Element-enriched Shergottites. *LPSC XXXIX*, abstract #1391.

Borg L. E., Brennecka G. A., and Symes S. J. (2016) Accretion timescale and impact history of Mars deduced from the isotopic systematics of martian meteorites: *Geochimica et Cosmochimica Acta,* **175**, 150-167.

Brennecka G. A., Borg L. E., and Wadhwa M. (2014) Insights into the Martian mantle: The age and isotopics of the meteorite fall Tissint. *Meteoritics & Planetary Science,* **49**, 412-418.

Brandon A. D., Nyquist L. E., Shih C. -Y., and Weismann H. (2004) Rb-Sr and Sm-Nd isotope systematics of shergottite NWA 856: Crystallization age and implications for alteration of hot desert SNC meteorites. *Lunar and Planetary Science Conference XXXV,* abstract #1931.

Bridges J. C., and Warren P. H. (2006) The SNC meteorites: basaltic igneous processes on Mars. *Journal of the Geological Society*, **163**, 229-25.

Cashman K. V., and Marsh B. D. (1988) Crystal size distribution (CSD) in rocks and the kinetics and dynamics of crystallization II: Makaopuhi lava lake. *Contributions to Mineralogy and Petrology,* **99**, 292-305.

Castle N., and Herd C. D. K. (2017) Experimental petrology of the Tissint meteorite: Redox estimates, crystallization curves, and evaluation of petrogenetic models. *Meteoritics & Planetary Science,* **52**, 125-146.

Christen F., Eugster O., and Busemann H., (2005) Mars ejection times and neutron capture effects of the nakhlites Y000593 and Y000749, the olivine-phyric shergottite Y980459, and the lherzolite NWA1950. *Antarctic Meteorite Research,* **18**, 117-132.

Crozaz G., Floss C., and Wadhwa M. (2003) Chemical alteration and REE mobilization in meteorites from hot and cold deserts. *Geochimica et Cosmochimica Acta*, **67**, 4727-4741.

Danyushevsky L. V., Della-Pasqua F. N., and Sokolov S. (2000) Re-equilibration of melt inclusions trapped by magnesian olivine phenocrysts from subduction-related magmas: petrological implications. *Contributions to Mineralogy and Petrology,* **138**, 68-83.

Danyushevsky L. V., Sokolov S., and Falloon T. J., (2002) Melt Inclusions in Olivine Phenocrysts: Using Diffusive Re-equilibration to Determine the Cooling History of a Crystal, with Implications for the Origin of Olivine-phyric Volcanic Rocks. *Journal of Petrology,* **43**, 1651-1671.

Danyushevsky L. V., and Plechov P. (2011) Petrolog3: Integrated software for modeling crystallization processes. *Geochemistry, Geophysics, Geosystems,* **12**, GC003516.

Day J. M. D., Corder C. S., Rumble D., Assayag N., Cartigny P., and Taylor L. A., (2015) Differentiation processes in FeO-rich asteroids revealed by the achondrite Lewis Cliff 88763. *Meteoritics & Planetary Science,* **50**, 1750-1766.

Debaille V., Yin Q. -Z., Brandon A. D., and Jacobsen B. (2008) Martian mantle mineralogy investigated by the ^{176}Lu-^{176}Hf and ^{147}Sm-^{143}Nd systematics of shergottites. *Earth and Planetary Science Letters,* **269**, 186-199.

Dreibus G., Spettel B., Haubold R., Jochum K. P., Palme H., Wolf D., and Zipfel J. (2000) Chemistry of a new shergottite: Sayh al Uhaymir 005. *Meteoritics & Planetary Science,* **35**, A49.

Ennis M. E., and McSween H. Y. (2014) Crystallization kinetics of olivine-phyric shergottites: *Meteoritics & Planetary Science,* **49**, 1440-1455.

Ferdous J., Brandon A. D., Peslier A. H., and Pirotte Z. (2017) Evaluating crustal contributions to enriched shergottites from the petrology, trace elements, and Rb-Sr and Sm-Nd isotope systematics of Northwest Africa 856: *Geochimica et Cosmochimica Acta,* **211**, 280-306.

Filiberto J., Musselwhite D. S., Gross J., Burgess K., Le L., and Treiman A. H. (2010) Experimental petrology, crystallization history, and parental magma characteristics of olivine-phyric shergottite NWA 1068: Implications for the petrogenesis of "enriched" olivine-phyric shergottites. *Meteoritics & Planetary Science*, **45**, 1258-1270.

Filiberto J., and Dasgupta R. (2011) Fe^{2+}-Mg partitioning between olivine and basaltic melts: Applications to genesis of olivine-phyric shergottites and conditions of melting in the Martian interior: *Earth and Planetary Science Letters,* **304**, 527-537.

Filiberto J., Gross J., Trela J. and Ferré E. C. (2014) Gabbroic Shergottite Northwest Africa 6963: An intrusive sample of Mars. *American Mineralogist,* **99**, 601-606.

Filiberto J. (2017) Geochemistry of Martian basalts with constraints on magma genesis. *Chemical Geology,* **466**, 1-14.

Ford C. E., Russell D. G., Craven J. A., and Fisk M. R. (1983) Olivine-Liquid Equilibria: Temperature, Pressure, and Composition Dependence of the Crystal/Liquid Cation Partition Coefficients for Mg, Fe^{2+}, Ca and Mn. *Journal of Petrology,* **24**, 256-266.

Ghiorso M. S., and Sack R. O. (1995) Chemical mass transfer in magmatic processes IV. A revised and internally consistent thermodynamic model for the interpolation and extrapolation of liquid-solid equilibria in magmatic systems at elevated temperatures and pressures. *Contributions to Mineralogy and Petrology*, **119**, 197-212.

Gillet P., Barrat J. A., Beck P., Marty B., Greenwood R. C., Franchi I. A., Bohn M., and Cotton J. (2005) Petrology, geochemistry, and cosmic-ray exposure age of lherzolitic shergottite Northwest Africa 1950: *Meteoritics & Planetary Science*, **40**, 1175-1184.

Gleason J. D., Kring D. A., Hill D. H., and Boynton W. V. (1997) Petrography and bulk chemistry of Martian lherzolite LEW88516: *Geochimica et Cosmochimica Acta,* **61**, 4007-4014.

Goodrich C. A., (2002) Olivine-phyric martian basalts: A new type of shergottite. *Meteoritics & Planetary Science*, **37**, B31–B34.

Goodrich C. A. (2003) Petrogenesis of olivine-phyric shergottites Sayh al Uhaymir 005 and Elaphant Moraine A79001 lithology A. *Geochimica et Cosmochimica Acta,* **67**, 3735-3771.

Goodrich C. A., Anne C., Herd C. D. K., and Taylor L. A., (2003) Spinels and oxygen fugacity in olivine-phyric and lherzolitic shergottites. *Meteoritics & Planetary Science*, **38**, 1773-1792.

Goodrich C. A., Treiman A. H., Filiberto J., Gross J., and Jercinovic M. (2013) K_2O-rich trapped melt in olivine in the Nakhla meteorite: Implications for petrogenesis of nakhlites and evolution of the Martian mantle. *Meteoritics & Planetary Science,* **48**, 2371-2405.

Greshake A., Fritz J., and Stöffler D. (2004) Petrology and shock metamorphism of the olivine-phyric shergottite Yamato 980459: Evidence for a two-stage cooling and single-stage ejection history. *Geochimica et Cosmochimica Acta,* **38**, 2359-2377.

Gross J., Filiberto J., Herd C. D. K., Daswani M. M., Schwenzer S. P., and Treiman A. H. (2013) Petrography, mineral chemistry, and crystallization history of olivine-phyric shergottite NWA 6234: A new melt composition. *Meteoritics & Planetary Science,* **48**, 854-871.

Harvey R. P., Wadhwa M., McSween H. Y., and Crozaz G. (1993) Petrography, mineral chemistry, and petrogenesis of Antarctic Shergottite LEW88516. *Geochimica et Cosmochimica Acta, 57*, 4769-4783

He Q., and Xiao L. (2014) Preliminary petrographic and melt-inclusion studies on the Northwest Africa 7397: Another enriched "lherzolitic" shergottite. *LPSC XXXXV,* abstract #1668.

Herd C. D. K., Papike J. J., and Brearley A. J. (2001) Oxygen fugacity of martian basalts from electron microprobe oxygen and TEM-EELS analyses of Fe-Ti oxides. *American Mineralogist, 86*, 1015-1024.

Herd C. D. K., Borg L. E., Jones J. H., and Papike J. J. (2002) Oxygen fugacity and geochemical variations in the martian basalts: Implications for martian basalt petrogenesis and the oxidation state of the upper mantle of Mars. *Geochimica et Cosmochimica Acta*, **66**, 2025–2036.

Herd C. D. K. (2003) The oxygen fugacity of olivine-phyric martian basalts and the components within the mantle and crust of Mars: *Meteoritics & Planetary Science, 38*, 1793-1805.

Herd C. D. K. (2006) Insights into the redox history of the NWA 1068/1110 martian basalt from mineral equilibria and vanadium oxybarometry. *American Mineralogist, 91*, 1616-1627.

Herd C. D. K., Walton E. L., Agee C. B., Muttik N., Ziegler K., Shearer C. K., Bell A. S., Santos A. R., Burger P. V., Simon J. I., Tappa M. J., McCubbin F. M., Gattacceca J., Lagroix F., Sanborn M. E., Yin Q. -Z., Cassata W. S., Borg L., Lindvall R. E., Kruijer T. S., Brennecka G. A., Kleine T., Nishiizumi K., and Caffee M. W. (2017) The Northwest Africa 8159 martian meteorite: Expanding the martian sample suite to the early Amazonian. *Geochimica et Cosmochimica Acta, 218*, 1-26.

Hewins R., and Zanda B. (2015) Northwest Africa 10169, The Meteorical Society. https://www.lpi.usra.edu/meteor/metbull.php?code=61969

Higgins M. D. (2000) Measurement of crystal size distributions. *American Mineralogist*, **85**, 1105-1116.

Higgins M. D. (2006) Quantitative Textural Measurements in Igneous and Metamorphic Petrology. *New York, Cambridge University Press*, 265

Higgins M. D. (2011) Textural coarsening in igneous rocks. *International Geology Review,* **53**, 354-376

Howarth G. H., Pernet-Fisher J. F., Balta J. B., Barry P. H., Bodnar R. J., and Taylor L. A. (2014) Two-stage polybaric formation of the new enriched pyroxene-oikocrystic, lherzolitic shergottite, NWA 7397. *Meteoritics & Planetary Science*, **49**, 1812-1830.

Howarth G. H., Pernet-Fisher J. F., Bodnar R. J., and Taylor L. A. (2015) Evidence for the exsolution of Cl-rich fluids in martian magmas: Apatite petrogenesis in the enriched lherzolitic shergottite Northwest Africa 7755. *Geochimica et Cosmochimica Acta*, **166**, 234-248.

Howarth G. H., and Udry A. (2017) Trace elements in olivine and the petrogenesis of the intermediate, olivine-phyric shergottite NWA 10170. *Meteoritics & Planetary Science,* **52**, 391-409.

Howarth G. H., Udry A., and Day J. M. D. (2018) Petrogenesis of basaltic shergottite Northwest Africa 8657: Implications for fO_2 correlations and element redistribution during shock melting shergottites. *Meteoritics & Planetary Science,* **53**, 249-267.

Hsu W., Guan Y., Wang H., Leshin L. A., Wang R., Zhang W., Chen X., Zhang F., and Lin C. (2004) The lherzolitic shergottite Grove Mountains 99027: Rare earth element geochemistry. *Meteoritics & Planetary Science*, **39**, 701-709.

Hui H., Peslier A., Lapen T. J., Shafer J. T., Brandon A. D., and Irving A. J. (2011) Petrogenesis of basaltic shergottite Northwest Africa 5298: Closed-system crystallization of an oxidized mafic melt. *Meteoritics & Planetary Science,* **46**, 1313-1328.

Ikeda Y. (1997) Petrology and mineralogy of the Y-793605 Martian meteorite. *Antarctic Meteorite Research,* **10**, 13.

Ikeda Y. (1998) Petrology of magmatic silicate inclusions in the Allan Hills 77005 lherzolitic shergottite. *Meteoritics & Planetary Science,* **33**, 803 – 812.

Jambon A., Barrat J. A., Sautter V., Gillet Ph., Göpel C., Javoy M., Joron J. L., and Lesourd M. (2002) The basaltic shergottite Northwest Africa 856: Petrology and chemistry: *Meteoritics & Planetary Science,* **37**, 1147-1164.

Jiang Y., and Hsu W. (2012) Petrogenesis of Grove Mountains 020090: An enriched "lherzolitic" shergottite. *Meteoritics & Planetary Science*, **47**, 1419-1435.

Lapen T. J., Mahlen N. J., Johnson C. M., and Beard B. L. (2004) High precision Lu and Hf isotope analyses of both spiked and unspiked samples: a new approach. *Geochemistry, Geophysics, Geosystems,* **5**, 2003GC000582.

Lapen T. J., Brandon A. D., Beard B. L., Peslier A. H., Lee C-T. A., and Dalton H. A. (2008) Lu-Hf age and isotope systematics of the olivine-phyric shergottite RBT-04262 and implications for the sources of enriched shergottites. *Lunar and Planetary Science Conference XXXIX,* abstract #2073.

Lapen T. J., Righter M., Brandon A. D., Beard B. L., Shafer J., and Irving A. J. (2009) Lu-Hf isotope systematics of NWA4468 and NWA2990: Implications for the sources of shergottites. *Lunar and Planetary Science Conference XXXX,* abstract #2376.

Lapen T. J., Righter M., Brandon A. D., Debaille V., Beard B. L., Shafer J. T., and Peslier A. H. (2010) A Younger Age for ALH84001 and Its Geochemical Link to Shergottite Sources in Mars. *Science*, **328**, 347-351.

Lapen T. J., Righter M., Andreasen R., Irving A. J., Satkoski A. M., Beard B. L., Nishiizumi K., Jull A. J. T., and Caffee M. W. (2017) Two billion years of magmatism recorded from a single Mars meteorite ejection site. *Science Advances,* **3**, e1600922.

Lin Y., Guan Y., Wang D., Kimura M., and Leshin L. A. (2005) Petrogenesis of the new lherzolitic shergottite Grove Mountains 99027: Constraints of petrography, mineral chemistry, and rare earth elements. *Meteoritics & Planetary Science*, **40**, 1599-1619.

Lin Y., Hu S., Miao B., Xu L., Liu Y., Xie L., Feng L., and Yang. J. (2013) Grove Mountains 020090 enriched lherzolitic shergottite: A two-stage formation model. *Meteoritics & Planetary Science,* **48**, 1572-1589.

Lodders K. (1998) A survey of shergottite, nakhlite and chassigny meteorites whole-rock compositions: *Meteoritics & Planetary Science*, **33**, A183-A190.

Marsh B. D. (1988) Crystal Size Distribution (CSD) in rocks and the kinetics and dynamics of crystallization, I. Theory. *Contributions to Mineralogy and Petrology,* **99**, 277-291.

Marsh B. D. (1998) On the interpretation of crystal size distributions in magmatic systems: *Journal of Petrology*, **39**, 553-599.

McCanta M. C., Beckett J. R., and Stolper E. M. (2016) Correlations and zoning patterns of phosphorus and chromium in olivine from H chondrites and the LL chondrite Semarkona. *Meteoritics & Planetary Science,* **51**, 520-546.

McSween H. Y., Stolper E. M., Taylor L. A., Muntean R. A., O'Kelley G. D., Eldridge J. S., Biswas S., Ngo H. T., and Lipschutz M. E. (1979) Petrogenetic relationship between Allan Hills 77005 and other achondrites. *Earth and Planetary Science Letters,* **45**, 275-284.

McSween H. Y., Eisenhour D. D., Taylor L. A., Wadhwa M., and Crozaz G. (1996) QUE 94201 shergottite: Crystallization of a Martian basaltic magma. *Geochimica et Cosmochimica Acta*, **60**, 4563-4569.

McSween H. Y., and Treiman A. H. (1998) Martian meteorites. *Reviews in Mineralogy,* **36**, 1-53.

McSween H. Y., Taylor G. J., and Wyatt M. B. (2009) Elemental Composition of the Martian Crust. *Science*, **324**, 736-739.

McSween H. Y. (2015) Petrology on Mars: *American Mineralogist,* **100**, 2380-2395.

Mikouchi T., and Miyamoto M. (1996) A new member of lherzolitic Shergottite from Japanes Antarctic Meteorite Collection: Mineralogy and petrology of Yamato-793605. *Antarctic Meteorites XXI,* **21**, 104-106.

Mikouchi T. (2005) Northwest Africa 1950: Mineralogy and comparison with Antarctic lherzolitic shergottites. *Meteoritics & Planetary Science,* **40**, 1621-1634.

Mikouchi T., and Kurihara T. (2008) Mineralogy and petrology of paired lherzolitic shergottites Yamato 000027, Yamato 000047, and Yamato 000097: Another fragment from a Martian "lherzolite" block. *Polar Science,* **2**, 175-194.

Milman-Barris M. S., Beckett J. R., Baker M. B., Hofmann A. E., Morgan Z., Crowley M. R., Vielzeuf D., and Stolper E. (2008) Zoning of phosphorus in igneous olivine: *Contributions to Mineralogy and Petrology,* **155**, 739-765.

Misawa K., Yamada K., Nakamura N., Morikawa N, Yamashita K., and Premo W. R. (2006) Sm-Nd isotope systematics of lherzolitic shergottite Yamato-793605. *Antarctic Meteorite Research,* **19**, 45-57.

Morgan D. J., and Jerram D. A. (2006) On estimating crystal shape for crystal size distribution analysis. *Journal of Volcanology and Geothermal Research*, **154**, 1-7.

Münker C., Weyer S., Scherer E., and Mezger K. (2001) Separation of high field strength elements (Nb, Ta, Zr, Hf) and Lu from rock samples for MC-ICP-MS measurements. *Geochemistry, Geophysics, Geosystems,* **2**, 2001GC000183.

Nekvasil H., Dondolini A., Horn J., Filiberto J., Long H., and Lindsley D. H. (2004) The origin and evolution of silica-saturated alkali suites: An experimental study. *Journal of Petrology*, **45**, 693-721.

Nekvasil H., Filiberto J., McCubbin F. M., and Lindsley D. H. (2007) Alkalic parental magmas for the chassignites?. *Meteoritics & Planetary Science*, **42**, 979-992.

Niihara T. (2011) Uranium-lead age of baddeleyite in shergottite Roberts Massif 04261: Implications for magmatic activity on Mars. *Journal of Geophysical Research: Planets*, **117**, E12

Nishiizumi K., and Caffee M. W. (2010) A tale of two shergottites: RBT 04261 and RBT 04262. *Lunar and Planetary Science Conference XXXXI,* abstract #2276.

Nyquist L. E., Bogard D. D., Shih C. –Y., Greshake A., Stöffler D., and Eugster O. (2001) Ages and Geologic Histories of Martian Meteorites. *Springer Netherlands*, **12**, 105-164.

Papike J. J., Karner J. M., Shearer C. K., and Burger P. V. (2009) Silicate mineralogy of martian meteorites *Geochimica et Cosmochimica Acta,* **73**, 7443-7485.

Platz T., Michael G., Tanaka K. L., Skinner J. A., and Fortezzo, C. M. (2013) Crater-based dating of geological units on Mars: Methods and application for the new global geological map. *Icarus*, **255**, 806–827.

Peslier A. H., Hnatyshin D., Herd C. D. K., Walton E. L., Brandon A. D., Lapen T. J., and Shafer J. T. (2010) Crystallization, melt inclusion, and redox history of a Martian meteorite: Olivine-phyric shergottite Larkman Nunatuk 06319. *Meteoritics & Planetary Science,* **74**, 4543 – 4576.

Peters T. J, Simon J. I., Jones J. H., Usui T., Moriwaki R., Economos R. C., Schmitt A. K., and McKeegan K. D. (2015) Tracking the source of the enriched martian meteorites in olivine-hosted melt inclusions of two depleted shergottites, Yamato 980459 and Tissint. *Earth and Planetary Science Letters*, **418**, 91-102.

Potter S. A., Brandon A. D., and Peslier A. H. (2015) Melt inclusion analysis of RBT 04262 with relationship to shergottites and Mars surface compositions. *Lunar and Planetary Science Conference XXXXVI,* Abstract #2945.

Rubin A. E., Warren P. H., Greenwood J. P., Verish R. S., Leshin L. A., Hervic R. L., Clayton R. N., and Mayeda T. K. (2000) Los Angeles: The most differentiated basaltic martian meteorite: *Geology,* **28**, 1011-1014.

Sack R. O. and Ghiorso M. S. (1989) Importance of considerations of mixing properties in establishing an internally consistent database: Thermochemistry of minerals in the system Mg2SiO4-Fe2SiO4-SiO2. *Contributions to Mineralogy and Petrology*, **102**, 41-68.

Sack R. O. and Ghiorso M. S. (1991a) An internally consistent model for the thermodynamic properties of Fe-Mg-titanomagnetite-aluminate spinels: Thermochemistry of minerals in the system Mg2SiO4-Fe2SiO4-SiO2. *Contributions to Mineralogy and Petrology,* **106**, 474-505.

Sack R. O. and Ghiorso M. S. (1991b) Chromian spinels as petrogenetic indicators: Thermodynamics and petrological applications. *American Mineralogist*, **76**, 827-847.

Sack R. O. and Ghiorso M. S. (1994a) Thermodynamics of multicomponent pyroxenes: I. Formulation of a general model. *Contributions to Mineralogy and Petrology*, **116**, 277-286.

Sack R. O. and Ghiorso M. S. (1994b) Thermodynamics of multicomponent pyroxenes: II. Phase relations in the quadrilateral. *Contributions to Mineralogy and Petrology*, **116**, 287-300.

Sack R. O. and Ghiorso M. S. (1994c) Thermodynamics of multicomponent pyroxenes: III. Calibration of $Fe^{2+}(Mg)_{-1}$, $TiAl_2(MgSi_2)_{-1}$, $TiFe_2^{3+}(MgSi_2)_{-1}$, $AlFe^{3+}(MgSi)_{-1}$, $NaAl(CaMg)_{-1}$, $Al_2(MgSi)_{-1}$ and $Ca(Mg)_{-1}$ exchange reactions between pyroxenes and silicate melts. *Contributions to Mineralogy and Petrology*, **118**, 271-296.

Shafer J. T., Brandon A. D., Lapen T. J., Righter M., Peslier A. H., and Beard B. L. (2010) Trace element systematics and ^{147}Sm-^{143}Nd and ^{176}Lu-^{176}Hf ages of Larkman Nunatak 06319: Closed-system fractional crystallization of an enriched shergottite magma *Geochimica et Cosmochimica Acta,* **74**, 7307-7328.

Shearer C. K., Aaron P. M., Burger P. V., Guan Y., Bell A. S., and Papike J. J. (2013) Petrogenetic linkages among fO_2, isotopic enrichments-depletions and crystallization history in Martian basalts. Evidence from the distribution of phosphorus in olivine megacrysts. *Geochimica et Cosmochimica Acta,* **120**, 17-38.

Shearer C. K., Burger P. V., Papike J. J., McCubbin F. M., and Bell A. S. (2015) Crystal chemistry of merrillite from Martian meteorites: Mineralogical recorders of magmatic processes and planetary differentiation. *Meteoritics & Planetary Science,* **50**, 649-673.

Shih C. -Y., Nyquist L. E., Weismann H., Reese Y., and Misawa K. (2005) Rb-Sr and Sm-Nd dating of olivine-phyric shergottite Yamato 980459: Petrogenesis of depleted shergottites. *Antarctic Meteorite Research,* **18**, 46-65.

Shih C. -Y., Nyquist L. E., Reese Y., and Misawa K. (2011) Sm-Nd and Rb-Sr studies of lherzolitic shergottite Yamato 984028. *Polar Science,* **4**, 515-529.

Smith P. M., and Asimow P. D. (2005) Adiabat_1ph: A new public front-end to the MELTS, pMELTS, and pHMELTS models. *Geochemistry, Geophysics, Geosystems,* **6**, GC000816.

Sonzogni Y., and Treiman A. H. (2015) Small melt inclusions can record bulk magma compositions: A planetary example from the Martian basalt (shergottite) Tissint. *Meteoritics & Planetary Science,* **50**, 1880-1895.

Stolper E., and McSween H. Y. (1979) Petrology and origin of the shergottite meteorites. *Geochimica et Cosmochimica Acta,* **43**, 1475-1477, 1479-1483, 1485-1498.

Symes S. J. K., Borg L. E., Shearer C. K., and Irving A. J. (2008) The age of the martian meteorite Northwest Africa 1195 and the differentiation history of the shergottites. *Geochimica et Cosmochimica Acta,* **72**, 1696–1710.

Takenouchi A., Mikouchi T., and Kogure T. (2017) Mineralogical study of brown olivine in Northwest Africa 1950 shergottite and implications for the formation mechanism of iron nanoparticles. *Meteoritics & Planetary Science,* **52**, 1-14.

Taylor L. A., Nazarov M. A., Shearer C. K., McSween H. Y., Cahill J., Neal C. R., Ivanova M. A., Barsukova L. D., Lentz R. C., Clayton R. N., and Mayeda T. K. (2002) Martian meteorite Dhofar 019: A new shergottite: *Meteoritics & Planetary Science,* **37**, 1107-1128.

Treiman A. H. (2003) Chemical compositions of martian basalts (shergottites): Some inferences on basalt formation, mantle metasomatism, and differentiation in Mars. *Meteoritics & Planetary Science,* **38**, 1849-1864.

Treiman A. H., and Filiberto J. (2015) Geochemical diversity of shergottite basalts: mixing and fractionation, and their relation to Mars surface basalts. *Meteoritics & Planetary Science,* **50**, 632-648.

Udry A., Howarth G. H., Lapen T. J., and Righter M. (2017) Petrogenesis of the NWA 7320 enriched martian gabbroic shergottite: Insight into the martian crust. *Geochimica et Cosmochimica Acta,* **204**, 1-18.

Usui T., Sanborn M., Wadhwa M., and McSween H. Y. (2010) Petrology and trace element geochemistry of Robert Massif 04261 and 04262 meteorites, the first examples of geochemically enriched lherzolitic shergottites. *Geochimica et Cosmochimica Acta*, **74**, 7283-7306.

Vervoort J. D., Patchett P. J., Söderlund U., and Baker M. (2004) Isotopic composition of Yb and the determination of Lu concentrations and Lu/Hf ratios by isotope dilution using MC-ICPMS. *Geochemistry, Geophysics, Geosystems,* **5**, GC000721.

Wadhwa M., McSween H. Y., and Floss C. (1994) Petrogenesis of shergottite meteorites inferred from minor and trace element microdistributions. *Geochimica et Cosmochimica Acta,* **58**, 4213-4229.

Walton E. L., Irving A. J., Bunch T. E., and Herd C. D. K. (2012) Northwest Africa 4797: A strongly shocked ultramafic poikilitic shergottite related to compositionally intermediate Martian meteorites. *Meteoritics & Planetary Science,* **47**, 1449-1474.

Watson E. B., Cherniak D. J., and Holycross M. E. (2015) Diffusion of phosphorus in olivine and molten basalt. *American Mineralogist,* **100**, 2053-2065.

Wieczorek M. A., and Zuber M. T. (2004) Thickness of the Martian crust: Improved constraints from geoid-to-topography ratios. *Journal of Geophysical Research*, **109**, E01009.

Wieler R., Huber L., Busemann H., Seiler S., Leya I., Maden C., Masarik J., Meier M. M. M., Nagao K., Trappitch R., and Irving A. J. (2016) Noble gases in 18 Martian meteorites and angrite Northwest Africa 7812 – Exposure ages, trapped gases, and a re-evaluation of the evidence for solar cosmic ray-produced neon in shergottites and other achondrites. *Meteoritics and Planetary Science*, **51**, 407-428.

Wood B. J. (1991) Oxygen barometry of spinel peridotites: *Reviews in Mineralogy*, **25**, 417-431.

Xing C. -M., Wang C. Y., and Tan W. (2017) Disequilibrium growth of olivine in mafic magmas revealed by phosphorus zoning patterns of olivine from mafic-ultramafic intrusions. *Earth and Planetary Science Letters,* **479**, 108-119

Zipfel J., Scherer P., Spettel B., Dreibus G., and Schultz L. (2000) Petrology and chemistry of the new shergottite Dar al Gani 476. *Meteoritics & Planetary Science,* **35**, 95-106.

Logan M. Combs

Department of Geoscience
University of Nevada, Las Vegas, NV 89154
lcombs1105@gmail.com

EDUCATION

University of Tennessee, Knoxville
Bachelors of Science, Geology, 2010-2014, *Summa Cum Laude*
3.91 GPA

University of Nevada, Las Vegas
Masters of Science, Geoscience, 2015-present
4.0 GPA

HONORS AND AWARDS

2018   **Lunar Planetary Institute (LPI) Career Development Award**
For outstanding first-author abstract submission to the 49th Lunar and Planetary Science
Conference
LPI: $1,000

2017   **Best Graduate Poster Presentation NVSGC 11th Annual Meeting**
Poster competition award.
Nevada Space Grant Consortium. Kindle Fire

2017   **Graduate Research Opportunity Fellowship**
Competitive NASA fellowship based on a written proposal.
Nevada Space Grant Consortium. $18,000

2016   **Second Place for Best Graduate Poster Presentation, 11th Annual UNLV
Geosymposium**
Competitive funding based on poster presentation for geoscience graduate students.
Kinross Gold Corporation. $200

2016   **Edwards & Olswang Geology Scholarship**
Competitive funding for geoscience graduate students.
Department of Geoscience, University of Nevada, Las Vegas. $250

2015   **Graduate Access Recruitment Award**
Award to recruit excellent graduate students.
Graduate College, Unversity of Nevada, Las Vegas. $1,000 per semester

2014   **Outstanding Student Presentation, Lunar and Planetary Science Conference, 2014**
Award for outstanding undergraduate student presentations.
Department of Earth and Planetary Sciences, University of Tennessee, Knoxville. $300

2014   **Don Byerly Field Camp Scholarship**
Competitive funding for undergraduate students attending field camp.
Department of Earth and Planetary Sciences, University of Tennessee, Knoxville. $2,000

2013   **Ann McInnis Undergraduate Student Award**
Award for excellent undergraduate geology students.
Knoxville Gem and Mineral Society. $250

2013   **Dawn M. Marsh Scholarship**
Competitive funding for undergraduates with high academic performance.
University of Tennessee, Knoxville. $1,200

RESEARCH AND EXPERIENCE

2017   **Hydrology Technician Intern, National Park Service**
Work with the Mojave Desert Network Inventories and Monitoring (MOJN I&M) program to perform water quality, flora and fauna surveys, and discharge measurements on desert springs in the 8 parks of the Mojave Desert Network. Install upland vegetation monitoring plots in Great Basin National Park.

2015-2017   **Master's Thesis**
Petrology of the new enriched lherzolitic shergotitte (NWA 10169): Insights into the martian interior
Project focusing on understanding the petrogenesis of the newly discovered lherzolitic shergottite NWA 10169. Goals of this project include constraining martian magmatic processes, and shergottite formation.

2013-2014   **Undergraduate Thesis**
A New H4/5 Ordinary Chondrite from North West Saudi Arabia, Al Jawf 001
Research project on the ordinary chondrite breccia Al Jawf 001, with Dr. Harry Y. McSween. Objectives were to classify, describe, and present findings at the 45th, Lunar and Planetary Science Conference

2010   **Summer Intern, Great Smoky Mountain National Park**
Recorded biological observations in the field with researchers, worked with fisheries, vegetation, and wildlife management departments, and assisted with elk reintroduction into Cataloochee, NC.

PUBLICATIONS AND EXTENDED ABSTRACTS

Combs, L. M., Udry, A., Howarth, G. H., Lapen, T. J., Righter, M., Gross, J., Day, J. M. D., & Rahib, R. R. (2018) Petrology and geochemistry of the enriched poikilitic shergottite Northwest Africa 10169: Insight into the martian interior. *49th Lunar and Planetary Science Conference,* Abstract #1727.

Rahib, R. R., Udry A., **Combs L. M.**, & Howarth, G. H. (2018) Formation and emplacement processes of martian poikilitic shergottite meteorites. *49th Lunar and Planetary Science Conference,* Abstract #1303.

Wilbur, Z. E., Udry, A., McCubbin, F. M., **Combs, L. M.**, Rahib, R. R., McCoy, T. J., & McCoy, C. (2018) Aubrite and enstatite chondrite impact melt meteorites as potential analogs to Mercury. *49th Lunar and Planetary Science Conference,* Abstract #1355.

Combs, L. M., Udry, A., & Day, J. M. D. (2016) Petrography and mineral chemistry of the new enriched lherzolitic shergottite, Northwest Africa 10169. *47th Lunar and Planetary Science Conference,* Abstract #2804.

Combs, L. M. & Gass, E. A. (2015) A New H4/5 Ordinary Chondrite from North West Saudi Arabia, Al Jawf 001, *Pursuit - The Journal of Undergraduate Research at the University of Tennessee*: V 6, Article 6.

Combs, L. M., Gass, E. A., McSween H. Y., Jahn, D. W., & Taylor L. A. (2014) Al Jawf 001, a new H-chondrite breccia, *45th Lunar and Planetary Science Conference,* Abstract #2481.

SKILLS

Analytical Equipment
Petrographic microscopes in both reflected and transmitted light, scanning electron microscope, electron microprobe (X-ray mapping, EDS and WDS point analysis), laser ablation system coupled with an inductively coupled plasma-mass spectrometer (LA-ICPMS).

Computer Software
Word, Powerpoint, Excel, Adobe Illustrator, Adobe Photoshop, ENVI, ArcGIS, ImageJ, AQUARIUS.

Relevant Coursework
Planetary Geology, Mineralogy, Igneous and Metamorphic Petrology, Structural Geology/Geophysics, Field Geology, Economic Geology, Sedimentology, Stable isotope geochemistry, and Radioactive isotope geochemistry

AFFILIATIONS

2017-present   Treasurer, UNLV SEG Chapter

2015-2017   Member, UNLV AAPG Chapter

2010-2017   Member, National Society of Collegiate Scholars

2011-2014   Member, University of Tennessee, Knoxville Geology Club